Available online at www.sciencedirect.com
ScienceDirect
Journal of Computational Physics 227 (2008) 2808–2844
JOURNAL OF COMPUTATIONAL PHYSICS
www.elsevier.com/locate/jcp

Dynamic transport simulation code including plasma rotation and radial electric field

M. Honda [*], A. Fukuyama

Department of Nuclear Engineering, Kyoto University, Kyoto 606-8501, Japan

Received 5 December 2006; received in revised form 29 October 2007; accepted 12 November 2007
Available online 22 November 2007

Abstract

A new one-dimensional transport code named TASK/TX, which is able to describe dynamic behavior of tokamak plasmas, has been developed. It solves simultaneously a set of flux-surface averaged equations composed of Maxwell's equations, continuity equations, equations of motion, heat transport equations, fast-particle slowing-down equations and two-group neutral diffusion equations. The set of equations describes plasma rotations in both toroidal and poloidal directions through momentum transfer and evaluates the radial electric field self-consistently. The finite element method with a piecewise linear interpolation function is employed with a fine radial mesh near the plasma surface. The Streamline Upwind Petrov–Galerkin method is also used for robust calculation. We have confirmed that the neoclassical properties are well described by the poloidal neoclassical viscous force. The modification of density profile during neutral beam injection is presented. In the presence of ion orbit loss, the generation of the inward radial electric field and torque due to radial current is self-consistently calculated.

PACS: 52.65.−y; 52.30.−q; 52.25.Fi; 52.55.Fa

Keywords: Transport simulation; Plasma rotation; Radial electric field; Finite element method; SUPG

---

1. Introduction

It has been widely recognized that improving plasma confinement and achieving high performance plasmas are crucially important for obtaining burning fusion plasma in ITER. The existence of transport barriers like an edge transport barrier (ETB) and/or an internal transport barrier (ITB) is considered to be indispensable to achieve and maintain high performance plasma. While various heat transport phenomena have been extensively studied both experimentally and theoretically so far and various theoretical models have been proposed

---

[*] Corresponding author. Present address: Japan Atomic Energy Agency, Naka, Ibaraki 311-0193, Japan. Tel.: +81 29 270 7352; fax: +81 29 270 7317.

E-mail address: honda.mitsuru@jaea.go.jp (M. Honda).

0021-9991/$ - see front matter © 2007 Elsevier Inc. All rights reserved.
doi:10.1016/j.jcp.2007.11.017

to explain and reproduce experimental observations, much less has been understood on particle transport. For instance, peaking and modification of a density profile during NBI heating require quantitative analyses.

The importance of radial electric field and plasma rotation in the transport barrier formation is now widely accepted. The quick transition from the L-mode to the H-mode (formation of ETB) is usually accompanied with a rapid change of a radial electric field. Since the radial electric field is strongly coupled with the plasma rotation through the radial force balance, the dynamic behavior of the transition is naturally regulated by an inertial term in an equation of motion. Therefore a dynamic analysis of the barrier formation requires to solve the equation of motion including the inertial term.

For conventional one-dimensional plasma transport analyses in toroidal plasmas, many researchers have been using a set of flux-surface averaged diffusion equations, which is based on the flux-gradient relation, associated with particle and heat flux. Many transport simulation codes based on this relation have been developed so far. Some of them, such as the TRANSP code [1], the ASTRA code [2] and the TASK/TR code [3], are able to describe the toroidal plasma rotation. The flux-gradient relation, however, implicitly assumes that the poloidal rotation is always in equilibrium. For transient phenomena, typically faster than the ion–ion collision time scale, it is necessary to solve the poloidal component of the equation of motion. We note that in this short time scale even the neoclassical transport flux is not ambipolar [4,5].

As for the description of the radial electric field E_r, three kinds of relations, which may govern it, have been used in the literatures. First, the radial force balance equation determines E_r mainly from the ion pressure gradient and the plasma rotation. Secondly, the radial electric field is generated by the radial current. The radial current equation, for singly charged ions, can be written as [6]

$$\frac{\epsilon_0\epsilon_\perp}{e}\frac{\partial}{\partial t}E_r = \Gamma_\mathrm{e} - \Gamma_\mathrm{i} \tag{1}$$

where ϵ_0 is the permittivity in a vacuum, $\epsilon_\perp$ the perpendicular dielectric constant and Γ_e and Γ_i the electron and ion particle fluxes. Finally E_r stems from only a little difference between the electron and ion densities through Gauss's law. In an equilibrium state or in the case of a slow change of a plasma, the force balance equation determines the radial electric field, while in the case of a rapid change the equation of motion perpendicular to both the radial direction and the magnetic field is reduced to Eq. (1) and determines the time evolution of E_r. Gauss's law provides the very little difference in electron and ion densities necessary for the radial electric field determined by other relations. Therefore it is obviously required that a self-consistent analysis including the time-evolution of the radial electric field and poloidal rotation should be carried out.

The purpose of this paper is to carry out a transport simulation describing the time-evolution of the radial electric field and plasma rotations self-consistently. We have newly developed a one-dimensional transport code TASK/TX, which mainly solves the flux-surface averaged two-fluid equations and the Maxwell's equations. The former equations consist of continuity equations, equations of motion in radial, poloidal and toroidal directions and heat transport equations for electrons and ions. The latter consist of Gauss's law (Poisson's equation), Faraday's law and Ampère's law. The behavior of fast-particles and neutrals is described by simple model equations. These equations are solved simultaneously. We describe the transport in the scrape-off layer (SOL), which is important for the formation of the edge transport barrier, using one-dimensional one-point model. We introduce the neoclassical effects into our code through the poloidal viscosity arising from the inhomogeneity of the magnetic field strength, although flux-surface averaged physical quantities are poloidally uniform. The poloidal viscosity induces the diffusion, resistivity, bootstrap current and Ware pinch. For the anomalous particle transport, we describe it as the momentum transfer between electrons and ions, while for the anomalous momentum and heat transport, we assume diffusive process with prescribed transport coefficient profiles.

Many of recent tokamak transport codes [1–3] employ the magnetic flux coordinates in a toroidal geometry. Since the primary purpose of the present paper is to demonstrate that a new set of transport equations actually works, however, we consider a tokamak plasma with a circular cross-section and a large aspect ratio to approximate it by a cylindrical plasma. Effects of the toroidal geometry and the non-circular cross-section will be taken into account in a subsequent paper, although we keep the poloidal viscosity due to the poloidal inhomogeneity of the magnetic field, as we mentioned in the previous paragraph. We employ a cylindrical coordinates (r, θ, ϕ), where r is the radial coordinate, θ the poloidal coordinate and ϕ the axial coordinate which corresponds to z/R with the axial length z and the periodic length $2\pi R$.

We adopt the finite element method (FEM) in order to solve the set of equations numerically. The advantages of the FEM are: (i) we can choose arbitrary size of space between the grid points, especially near the plasma surface. (ii) various kinds of boundary conditions can be implemented without difficulty, (iii) it is easy to implement the upwind technique in order to improve the numerical stability in the advection equation. In order to comfortably impose the boundary conditions at the magnetic axis, we choose $s = r^2$ as the radial coordinate in computation. Removing the first-order derivatives in terms of electrostatic and electromagnetic potentials enhances the numerical stability. For the radial component of the equations of motion still keeping the first derivative terms, we have introduced the Streamline Upwind Petrov–Galerkin (SUPG) method [7]. This method substantially suppresses numerical errors and thus improves the numerical stability.

The remainder of this paper is organized as follows. Section 2 describes the basic equations of the TASK/TX code and the physics contained in the code. Section 3 presents the numerical method to solve the basic equations. In Section 4, we demonstrate typical calculation results in a few situations and comparison of the neoclassical effects against the analytic models. We also present the density profile modification due to NBI and the effects of ion orbit loss. Conclusion and discussion are given in Section 5.

2. Transport models

2.1. Basic equations

We start from the collisional two-fluid equations derived by Braginskii [8]; the continuity equation, the equations of motion, and the thermal transport equation. The terms of momentum exchange, perpendicular viscosity, and thermal diffusivity come from not only the particle collisions but also the interactions with turbulence.

Since the transport of particles and heat along the magnetic field line is much faster than that across the flux surfaces, the variation of physical quantities on a magnetic surface is small, ρ_{i}/L and ν/Ω where ρ_{i} is the ion thermal Larmor radius, L the radial scale length, ν the collisionality and Ω the cyclotron frequency [9]. This is equivalent to an expansion in the ratio of perpendicular to parallel heat conductivity or diffusion coefficients. Therefore we consider the flux-surface averaged quantities: $X(r,t) \equiv (1/4\pi^2)\int_0^{2\pi} \mathrm{d}\theta \int_0^{2\pi} \mathrm{d}\phi \widetilde{X}(r,\theta,\phi,t)$. By integrating the two-fluid equations over θ and ϕ, we obtain a flux-surface averaged two-fluid equations in the lowest order of ρ_{i}/L and ν/Ω. More detail of the derivation is given in Appendix A.

We keep the poloidal viscosity, which stems from the poloidal asymmetry of the magnetic field strength [9], because it plays an important role in producing the neoclassical transport. Finally we assume that the plasma is composed of electrons, bulk ions, beam ions and neutrals; impurities are neglected in the present analysis, for simplicity.

For electrons and bulk ions, the one-dimensional two-fluid equations of motion are taken for the radial flow u_{sr}, poloidal and toroidal rotations $u_{s\theta}$ and $u_{s\phi}$, in addition to the continuity and the heat transport equations for the density n_s and the internal energy $3/2n_sT_s$ as follows:

$$\frac{\partial n_s}{\partial t} = -\frac{1}{r}\frac{\partial}{\partial r}(rn_su_{sr}) + S_s, \tag{2}$$

$$\frac{\partial}{\partial t}(m_sn_su_{sr}) = -\frac{1}{r}\frac{\partial}{\partial r}(ru_{sr}m_sn_su_{sr}) + \frac{1}{r}m_sn_su_{s\theta}^2 + e_sn_s(E_r + u_{s\theta}B_\phi - u_{s\phi}B_\theta) - \frac{\partial}{\partial r}(n_sT_s), \tag{3}$$

$$\begin{aligned}\frac{\partial}{\partial t}(m_sn_su_{s\theta}) = {}& -\frac{1}{r^2}\frac{\partial}{\partial r}(r^2u_{sr}m_sn_su_{s\theta}) + \frac{1}{r^2}\frac{\partial}{\partial r}\left[r^3m_sn_s\mu_s\frac{\partial}{\partial r}\left(\frac{u_{s\theta}}{r}\right)\right] + e_sn_s(E_\theta - u_{sr}B_\phi) + F_{s\theta}^{\mathrm{NC}} + F_{s\theta}^{\mathrm{C}} \\ & + F_{s\theta}^{\mathrm{W}} + F_{s\theta}^{\mathrm{L}} + F_{s\theta}^{\mathrm{N}} + F_{s\theta}^{\mathrm{CX}},\end{aligned} \tag{4}$$

$$\begin{aligned}\frac{\partial}{\partial t}(m_sn_su_{s\phi}) = {}& -\frac{1}{r}\frac{\partial}{\partial r}(ru_{sr}m_sn_su_{s\phi}) + \frac{1}{r}\frac{\partial}{\partial r}\left(rm_sn_s\mu_s\frac{\partial u_{s\phi}}{\partial r}\right) + e_sn_s(E_\phi + u_{sr}B_\theta) + F_{s\phi}^{\mathrm{C}} + F_{s\phi}^{\mathrm{W}} + F_{s\phi}^{\mathrm{L}} \\ & + F_{s\phi}^{\mathrm{N}} + F_{s\phi}^{\mathrm{CX}},\end{aligned} \tag{5}$$

$$\frac{\partial}{\partial t}\left(\frac{3}{2}n_sT_s\right) = -\frac{1}{r}\frac{\partial}{\partial r}\left(\frac{5}{2}ru_{sr}n_sT_s\right) + \frac{1}{r}\frac{\partial}{\partial r}\left(rn_s\chi_s\frac{\partial T_s}{\partial r}\right) + u_{sr}\frac{\partial}{\partial r}n_sT_s + e_sn_s(E_\theta u_{s\theta} + E_\phi u_{s\phi}) + P_s^{\mathrm{C}} + P_s^{\mathrm{B}} + P_s^{\mathrm{L}} + P_s^{\mathrm{R}} + P_s^{\mathrm{RF}}, \tag{6}$$

where the subscript s denotes the particle species and m_s and e_s are the mass and charge, respectively. The perpendicular viscosity μ_s and thermal conductivity χ_s represent anomalous transport due to turbulence. The particle source S_s, neoclassical viscous force F_s^{NC}, classical collisional momentum transfer F_s^{C}, forces due to the interaction with turbulent electric field F_s^{W}, parallel transport loss in the SOL region F_s^{L}, friction force with neutrals F_s^{N}, charge exchange force F_s^{CX}, collisional energy transfer power P_s^{C}, heating power from NBI P_s^{B}, collisional energy loss power P_s^{L}, bremsstrahlung power P_s^{R} and direct RF heating power P_s^{RF} are calculated with local quantities and will be explained in detail later.

Next we consider the equations for beam ions. In our transport model, the momentum input from NBI increases the toroidal velocity of beam ions and then through collisional momentum transfer between thermal species and beam ions net heating terms emerge in heat transport equations. For the beam ions, the radial convection and diffusion are usually much slower than the slowing-down process and neglected for simplicity. We consider the equations of the beam ion density n_{b} produced by the neutral beam and the poloidal and toroidal rotations $u_{\mathrm{b}\theta}$ and $u_{\mathrm{b}\phi}$, written in the form

$$\frac{\partial n_{\mathrm{b}}}{\partial t} = S_{\mathrm{b}}, \tag{7}$$

$$\frac{\partial}{\partial t}(m_{\mathrm{b}}n_{\mathrm{b}}u_{\mathrm{b}\theta}) = e_{\mathrm{b}}n_{\mathrm{b}}E_\theta + F_{\mathrm{b}\theta}^{\mathrm{C}} + F_{\mathrm{b}\theta}^{\mathrm{L}} + F_{\mathrm{b}\theta}^{\mathrm{N}} + F_{\mathrm{b}\theta}^{\mathrm{CX}}, \tag{8}$$

$$\frac{\partial}{\partial t}(m_{\mathrm{b}}n_{\mathrm{b}}u_{\mathrm{b}\phi}) = e_{\mathrm{b}}n_{\mathrm{b}}E_\phi + F_{\mathrm{b}\phi}^{\mathrm{C}} + F_{\mathrm{b}\phi}^{\mathrm{L}} + F_{\mathrm{b}\phi}^{\mathrm{N}} + F_{\mathrm{b}\phi}^{\mathrm{CX}} + F_{\mathrm{b}\phi}^{\mathrm{B}}, \tag{9}$$

where $F_{\mathrm{b}\phi}^{\mathrm{B}}$ denotes the momentum input from the beam neutrals.

Neutrals in a plasma have a crucial role to determine the plasma density through ionization and the ion momentum and energy loss through charge exchange. The velocity distribution function of neutrals is actually important and the Monte Carlo method is usually used for neutral transport analyses. For simplicity, however, in the present code we describe the behavior of two-group neutrals by a set of diffusion equations: one is slow neutrals with the order of room temperature and the other is fast neutrals with the order of ion temperature. Frequent charge exchange reactions between neutrals and plasma ions lead to a random walk and then diffusion to the center of the plasma [10].

We therefore solve the diffusion equations for two-group neutrals composed of slow and fast neutrals, n_{01} and n_{02}, respectively, in the form

$$\frac{\partial n_{0s}}{\partial t} = \frac{1}{r}\frac{\partial}{\partial r}\left(rD_{0s}\frac{\partial n_{0s}}{\partial r}\right) + S_{0s}, \tag{10}$$

where the subscript $0s$ denotes the neutral species of slow ($s = 1$) or fast ($s = 2$) and S_{0s} is the sum of the source and sink term which will be given in Eqs. (29) and (30).

As already mentioned in Section 1, the radial electric field plays a very important role in describing rapid phenomena and plasma rotations self-consistently. In order to take into account the formation of the radial electric field, we should consider the charge separation. The loss of fast particles also induces the charge separation. We do not assume the quasi charge neutrality but solve the Poisson's equation. When the time variation of the charge density is not zero, we have to keep the displacement current in Ampère's law because $\nabla\cdot\vec{j} \neq 0$, where j denotes the current density. Based on the above consideration, we should finally couple the transport equations with the averaged Maxwell's equations composed of the Poisson's equation, Faraday's law and Ampère's law for the radial, poloidal and toroidal electric fields, E_r, E_θ and E_ϕ, and the poloidal and toroidal magnetic fields B_θ and B_ϕ as follows:

$$\frac{1}{r}\frac{\partial}{\partial r}(rE_r) = \frac{1}{\epsilon_0}\sum_s e_sn_s, \tag{11}$$

$$\frac{1}{c^2}\frac{\partial E_\theta}{\partial t} = -\frac{\partial B_\phi}{\partial r} - \mu_0 \sum_s e_s n_s u_{s\theta}, \tag{12}$$

$$\frac{1}{c^2}\frac{\partial E_\phi}{\partial t} = \frac{1}{r}\frac{\partial}{\partial r}(rB_\theta) - \mu_0 \sum_s e_s n_s u_{s\phi}, \tag{13}$$

$$\frac{\partial B_\theta}{\partial t} = \frac{\partial E_\phi}{\partial r}, \tag{14}$$

$$\frac{\partial B_\phi}{\partial t} = -\frac{1}{r}\frac{\partial}{\partial r}(rE_\theta), \tag{15}$$

where μ_0 is the permeability in a vacuum and c is the speed of light.

As will also be discussed in Section 3.5, spatial second-order derivatives are more favorable than first-order derivatives from a numerical stability point of view; we therefore employ a form of Maxwell's equations without first-order derivatives by the use of electrostatic and electromagnetic potentials,

$$0 = \frac{1}{r}\frac{\partial}{\partial r}\left(r\frac{\partial \Phi}{\partial r}\right) + \frac{1}{\epsilon_0}\sum_s e_s n_s, \tag{16}$$

$$\frac{1}{c^2}\frac{\partial \dot{A}_\theta}{\partial t} = \frac{\partial}{\partial r}\left[\frac{1}{r}\frac{\partial}{\partial r}(rA_\theta)\right] + \mu_0 \sum_s e_s n_s u_{s\theta}, \tag{17}$$

$$\frac{1}{c^2}\frac{\partial \dot{A}_\phi}{\partial t} = \frac{1}{r}\frac{\partial}{\partial r}\left(r\frac{\partial A_\phi}{\partial r}\right) + \mu_0 \sum_s e_s n_s u_{s\phi}, \tag{18}$$

$$\frac{\partial A_\phi}{\partial t} = \dot{A}_\phi, \tag{19}$$

$$\frac{\partial A_\theta}{\partial t} = \dot{A}_\theta, \tag{20}$$

where Φ is the electrostatic potential, A_θ and A_ϕ the poloidal and toroidal electromagnetic potentials. Eqs. (19) and (20) are the definitions of $\dot{A}_\phi$ and $\dot{A}_\theta$. The relations between fields and potentials are given by

$$\begin{aligned} &E_r = -\frac{\partial \Phi}{\partial r}; \quad E_\theta = -\frac{\partial A_\theta}{\partial t} = -\dot{A}_\theta; \quad E_\phi = -\frac{\partial A_\phi}{\partial t} = -\dot{A}_\phi; \\ &B_\theta = -\frac{\partial A_\phi}{\partial r}; \quad B_\phi = \frac{1}{r}\frac{\partial}{\partial r}(rA_\theta). \end{aligned} \tag{21}$$

By solving a set of 20 equations simultaneously, we describe the time-evolution of a tokamak plasma and, thus, various waves in a plasma can be potentially described. In the present model, however, the plasma oscillation and the shear Alfvén waves never appear because $k_\parallel = 0$ for flux-surface averaged quantities. Other electromagnetic waves, O and X waves, have frequencies higher than MHz. Since we use full-implicit method as the time integration method as will be described in Section 3.4, we can ignore these waves for a time step $\gtrsim 10^{-6}$ s. Therefore we can simulate and clarify the plasma behavior in transport time scales.

2.2. Physics models in the model equations

2.2.1. Particle source

The particle source terms in Eqs. (2) and (7) are written as follows:

$$S_\mathrm{e} = (n_{01} + n_{02})\langle\sigma_\mathrm{ion} v\rangle n_\mathrm{e} - S_\mathrm{e}^\mathrm{L} + (1 - f_\mathrm{CX})\frac{P_\mathrm{b}}{E_\mathrm{b}}, \tag{22}$$

$$S_\mathrm{i} = \frac{1}{Z_\mathrm{i}}(n_{01} + n_{02})\langle\sigma_\mathrm{ion} v\rangle n_\mathrm{e} - f_\mathrm{CX}\frac{P_\mathrm{b}}{E_\mathrm{b}} + \nu_\mathrm{b} n_\mathrm{b} - S_\mathrm{i}^\mathrm{L}, \tag{23}$$

$$S_\mathrm{b} = \frac{P_\mathrm{b}}{E_\mathrm{b}} - \nu_\mathrm{b} n_\mathrm{b} - S_\mathrm{b}^\mathrm{L}, \tag{24}$$

where $\sigma_{\rm ion}$ is the ionization cross section and thus $\langle\sigma_{\rm ion}v\rangle$ denotes the ionization rate, $Z_{\rm i}$ the charge of ions, and $S_{\rm e}^{\rm L}$ and $S_{\rm b}^{\rm L}$ the electron and beam ion losses due to parallel transport in the SOL region, which will be explained in detail in the next section. $S_{\rm i}^{\rm L}$ also denotes the ion parallel loss in the SOL and is connected with $S_{\rm e}^{\rm L}$ and $S_{\rm b}^{\rm L}$ through the relation

$$S_{\rm e}^{\rm L} = Z_{\rm i}S_{\rm i}^{\rm L} + Z_{\rm b}S_{\rm b}^{\rm L}.$$

There are three basic atomic processes leading to beam neutral absorption: charge exchange with the cross-section $\sigma_{\rm CX}$, ionization by ions with $\sigma_{\rm ion}$, and ionization by electrons [10]. These processes have different cross-sections dependent on the energy of injected beam atoms. In general, the cross-section of electron ionization is negligible because it is much smaller than $\sigma_{\rm CX}$ in lower energy range, typically $\lesssim 100$ keV, and also smaller than $\sigma_{\rm ion}$ in higher energy range, typically $\gtrsim 50$ keV. Then the processes that we now consider in the code are, using subscripts b for beam,

$$\begin{array}{ll}\text{Charge exchange} & D_{\rm b} + D^+ \rightarrow D_{\rm b}^+ + D\\ \text{Ionization by ions} & D_{\rm b} + D^+ \rightarrow D_{\rm b}^+ + D^+ + {\rm e}.\end{array}$$

Below about 90 keV, charge exchange is the most effective process for a deuterium beam. Above this energy, however, ionization by ions becomes dominant. The cross-section of the charge exchange is given by [11]

$$\sigma_{\rm CX} = \frac{6.937\times 10^{-19}(1-0.155\log_{10}\widehat{E})}{1+0.1112\times 10^{-14}\widehat{E}^{3.3}}, \tag{25}$$

where $\widehat{E}$ is defined as $\widehat{E} = E/A_{\rm i}$, and E denotes the energy of the interesting species and $A_{\rm i}$ denotes its atomic mass number. The cross-section of the ion ionization is expressed as

$$\begin{aligned}&\sigma_{\rm ion} = 3.6\times 10^{-16}\frac{\log_{10}(0.1666\widehat{E})}{\widehat{E}}, \quad \text{for } \widehat{E} > 150\ \text{keV}\\ &\log_{10}\sigma_{\rm ion} = -0.8712(\log_{10}\widehat{E})^2 + 8.156\log_{10}\widehat{E} - 38.833, \quad \text{for } \widehat{E} < 150\ \text{keV}.\end{aligned}$$

Therefore the fraction of charge exchange process $f_{\rm CX}$ is given by $f_{\rm CX} = \sigma_{\rm CX}/(\sigma_{\rm CX}+\sigma_{\rm ion})$.

The power deposition density and the beam energy are expressed by $P_{\rm b}$ and $E_{\rm b}$, respectively. The quantity $P_{\rm b}/E_{\rm b}$ represents the number density of ions kicked by the beam neutrals per second. The slowing-down rate of the beam ions $\nu_{\rm b}$ is given by [12]

$$\nu_{\rm b} = \frac{3}{2}\nu_{\rm be}\left\{\ln\left[1+\left(\frac{E_{\rm b}}{E_{\rm c}}\right)^{3/2}\right]\right\}^{-1}$$

where $\nu_{\rm be}$ is the collisionality of beam ions with electrons and will be given in Section 2.2.3. $E_{\rm c}$ is the critical beam energy

$$E_{\rm c} = \left(\frac{3\pi^{1/2}}{4}\right)^{2/3}\left(\frac{m_{\rm i}}{m_{\rm e}}\right)^{1/3}\frac{m_{\rm b}}{m_{\rm i}}T_{\rm e},$$

and the electron and ion heating rates are equal when $E_{\rm b} = E_{\rm c}$.

In present tokamaks, there are two types of NBI systems: tangential NBI and perpendicular NBI. The former contributes to not only the collisional heating but also the momentum input, while the latter contributes to only the heating. The TASK/TX code assumes that the tangential NBI gives the momentum to the background plasma only in the toroidal direction. Then the injection rate of toroidal momentum is expressed as

$$F_{{\rm b}\phi}^{\rm B} = m_{\rm b}v_{\rm b}\frac{P_{{\rm b}\|}}{E_{\rm b}},$$

where $P_{{\rm b}\|}$ is the tangential component of the NBI power.

As for the ionization rate, we employ an approximate expression [13]

$$\langle\sigma_{\text{ion}}v\rangle = \frac{10^{-11}(T_{\text{e}}/U_{\text{ion}})^{1/2}}{U_{\text{ion}}^{3/2}(6+T_{\text{e}}/U_{\text{ion}})}\exp(-U_{\text{ion}}/T_{\text{e}}),$$

where U_{ion} is the ionization energy and T_{e} and U_{ion} both in eV. We note that this expression is valid for $0.02 \lesssim T_{\text{e}}/U_{\text{ion}} \lesssim 100$.

The charge exchange collision between ions and neutrals causes the momentum loss of ions, although the total particle number of ions and neutrals does not change. By using Eq. (25), the charge exchange rate has been approximated as

$$\langle\sigma_{\text{CX}}v\rangle = \sigma_{\text{CX}}\left(\frac{8T_{\text{i}}}{\pi m_{\text{i}}}\right)^{1/2}.$$

The charge exchange forces acting on ions are expressed as

$$\begin{aligned}
F_{\text{i}\theta}^{\text{CX}} &= -n_{\text{i}}m_{\text{i}}(n_{01}+n_{02})\langle\sigma_{\text{CX}}v\rangle u_{\text{i}\theta},\\
F_{\text{i}\phi}^{\text{CX}} &= -n_{\text{i}}m_{\text{i}}(n_{01}+n_{02})\langle\sigma_{\text{CX}}v\rangle u_{\text{i}\phi},\\
F_{\text{b}\theta}^{\text{CX}} &= -n_{\text{i}}m_{\text{i}}(n_{01}+n_{02})\langle\sigma_{\text{CX}}v\rangle u_{\text{b}\theta},\\
F_{\text{b}\phi}^{\text{CX}} &= -n_{\text{i}}m_{\text{i}}(n_{01}+n_{02})\langle\sigma_{\text{CX}}v\rangle u_{\text{b}\phi}.
\end{aligned}$$

2.2.2. Particle loss and recycling in the SOL

While in a plasma inside the last closed flux surface (LCFS) all the magnetic field lines are confined, field lines in a SOL region no longer make closed flux surfaces and a SOL plasma flows along the field lines towards the poloidal limiter or divertor. In order to describe this parallel transport, we introduce particle, momentum and heat losses in the SOL region of $a < r < b$, where a and b are the minor radius of the plasma and of the wall, respectively.

Since it requires long computation time to solve a two-dimensional fluid equation, various kinds of reduced models have been proposed to analyze the transport in the SOL. It is reported that the two-point model for SOL and divertor plasmas based on integral fluid equations can easily reproduce static characteristics observed in experiments [14]. The two-point model is also suitable for coupling with the core transport code [15]. Since the model cannot deal with the poloidal asymmetry of the SOL, the five-point model [16] has been recently proposed. In the present analysis, however, the major purpose to describe the SOL together with the core is to provide appropriate boundary conditions at the plasma surface and to analyze the radial structure of transition region between the core and SOL. We therefore employ a simple one-point model.

It is found in some papers that this one-point model has been used coupled with the transport code to solve a whole plasma [17,18]. In these simulations, convection loss mechanism is considered for particle and heat losses. The mechanism of the electron heat loss is, however, governed by a different physics, conduction, so that the heat transport in the SOL is much faster than the particle transport. We then include both convective and conductive loss mechanisms in our model.

It is now assumed that the particle loss time is proportional to the distance from the plasma surface to the divertor along the field line divided by the ion sound speed $C_{\text{s}} \equiv (Z_{\text{i}}T_{\text{e}}/m_{\text{i}} + 3T_{\text{i}}/m_{\text{i}})^{1/2}$. Based on this assumption, the particle loss rate can be evaluated as

$$\nu_{\text{L}} = \frac{k_{\text{L}}C_{\text{s}}}{L}g(r),$$

where k_{L} is the numerical factor alleviating the sound speed, L is the characteristic length in the direction of the magnetic field line in the SOL given by $2\pi qR$ and $g(r)$ is a smoothing function chosen for stable numerical calculation. From observations in experiments, $k_{\text{L}} = 0.3$ is usually chosen [19]. If $g(r) = 1$, the magnitude of ν_{L} jumps up at the plasma surface because $\nu_{\text{L}} = 0$ in the core and this causes a serious numerical problem in the FEM analysis. To avoid the problem, we have introduced the smoothing function $g(r)$, given by

$$g(r) = \frac{\rho^2}{1+\rho^2},$$

where $\rho \equiv (r-a)/\delta$ for $r \geqslant a$ and $\rho \equiv 0$ for $r < a$, and δ is typically chosen as the order of the banana width.

According to Spitzer and Härm [20], the electron heat conduction along the field line can be written as [14],

$$q_{\mathrm{e}\|}(\ell) = -\kappa_0 T_{\mathrm{e}}^{5/2}\frac{\partial T_{\mathrm{e}}}{\partial \ell}, \tag{26}$$

where $q_{\mathrm{e}\|}$ is the parallel heat flux density, ℓ is the distance along the magnetic field line and

$$\kappa_0 = \frac{(4\pi\epsilon_0)^2}{m_{\mathrm{e}}^{1/2} Z_{\mathrm{eff}} e^4 \ln \Lambda_{\mathrm{e}}}, \tag{27}$$

where Z_{eff} is the effective charge of the plasma and $\ln \Lambda_{\mathrm{e}}$ the Coulomb logarithm of electron collisions defined by [21]

$$\ln \Lambda_{\mathrm{e}} = 37.8 - \frac{1}{2}\ln\left(\frac{n_{\mathrm{e}}}{\mathrm{m}^{-3}}\right) + \ln\left(\frac{T_{\mathrm{e}}}{\mathrm{keV}}\right). \tag{28}$$

If we assume that $q_{\mathrm{e}\|}$ is used in a heat diffusion equation and the scale length of the temperatures is represented by L, we obtain the electron heat loss rate

$$\nu_{\mathrm{L}T_{\mathrm{e}}} = k_{\mathrm{L}T_{\mathrm{e}}}\frac{\kappa_0 T_{\mathrm{e}}^{5/2}}{L^2 n_{\mathrm{e}}} g(r),$$

where $k_{\mathrm{L}T_{\mathrm{e}}}$ the numerical factor which in our case is taken as unity. As in the case of the particle loss, $\nu_{\mathrm{L}T_{\mathrm{e}}}$ is multiplied by the alleviation function $g(r)$.

When we consider the case of the ion heat loss, from Eq. (27) κ_0 of ions is obviously smaller than that of electrons by a factor of the square root of mass ratio and the magnitude of the ion conduction becomes the same order as that of the convection. It is therefore reasonable that we assume the convective form of the ion heat loss as

$$\nu_{\mathrm{L}T_{\mathrm{i}}} = \frac{k_{\mathrm{L}T_{\mathrm{i}}} C_{\mathrm{s}}}{L} g(r),$$

and we usually choose $k_{\mathrm{L}T_{\mathrm{i}}} = 1$.

Using the above-defined loss rates, the loss terms in Eqs. (22), (23), (4)–(6) can be expressed as

$$\begin{aligned}
S_{\mathrm{e}}^{\mathrm{L}} &= -\nu_{\mathrm{L}}(n_{\mathrm{e}} - n_{\mathrm{ediv}}),\\
F_{s\theta}^{\mathrm{L}} &= -2\nu_{\mathrm{L}} n_s u_{s\theta},\\
F_{s\phi}^{\mathrm{L}} &= -2\nu_{\mathrm{L}} n_s u_{s\phi},\\
P_s^{\mathrm{L}} &= T_s\frac{S_{\mathrm{e}}^{\mathrm{L}}}{Z_s} - \frac{3}{2}\nu_{\mathrm{L}T_s} n_s (T_s - T_{s\mathrm{div}})
\end{aligned}$$

where we have introduced the electron density and electron and ion temperatures in the divertor region, n_{ediv} and $T_{s\mathrm{div}}$, respectively, to sustain a dilute plasma in the SOL. The numerical factor of two appeared in the momentum loss terms stems from the sum of the contributions from the density and velocity losses. The heat loss term is a sum of the convective loss and the conductive loss.

Losses of the momentum equations consist of not only the loss to the divertor in the SOL but also the friction forces due to collisions with neutrals. We can express this frictional loss term as

$$\begin{aligned}
F_{s\theta}^{\mathrm{N}} &= -n_s m_s (n_{01} + n_{02})\langle\sigma_0 v\rangle u_{s\theta},\\
F_{s\phi}^{\mathrm{N}} &= -n_s m_s (n_{01} + n_{02})\langle\sigma_0 v\rangle u_{s\phi},\\
F_{\mathrm{b}\theta}^{\mathrm{N}} &= -n_{\mathrm{b}} m_{\mathrm{b}} (n_{01} + n_{02})\langle\sigma_0 v\rangle u_{\mathrm{b}\theta},\\
F_{\mathrm{b}\phi}^{\mathrm{N}} &= -n_{\mathrm{b}} m_{\mathrm{b}} (n_{01} + n_{02})\langle\sigma_0 v\rangle u_{\mathrm{b}\phi},
\end{aligned}$$

where $\sigma_0 = 8.8 \times 10^{-21}\mathrm{m}^2$ is the characteristic atomic collision cross section [21].

Furthermore, we assume that ions reaching the divertor along the field lines are reflected back as neutral particles with recycling rate γ_0 and thus are led to use the following expression for the particle sources in the diffusive transport equations for slow and fast neutrals

$$S_{01} = -\frac{1}{Z_\mathrm{i}} n_{01}\langle\sigma_\mathrm{ion}v\rangle n_\mathrm{e} - n_{01}\langle\sigma_\mathrm{CX}v\rangle n_\mathrm{i} + \frac{\gamma_0}{Z_\mathrm{i}}v_\mathrm{L}(n_\mathrm{e} - n_\mathrm{ediv}), \tag{29}$$

$$S_{02} = -\frac{1}{Z_\mathrm{i}} n_{02}\langle\sigma_\mathrm{ion}v\rangle n_\mathrm{e} + n_{01}\langle\sigma_\mathrm{CX}v\rangle n_\mathrm{i} + f_\mathrm{CX}\frac{P_\mathrm{b}}{E_\mathrm{b}}. \tag{30}$$

The first terms in both formulae express the reduction of number of neutrals due to ionization, leading to the increase in electron and ion densities. The second terms represent annihilation and generation of fast neutrals due to charge exchange, and the last term of Eq. (30) denotes the neutral source from the NBI. In addition, we include the effect of gas puff with the influx rate Γ_0 of neutrals from the wall as a boundary condition of Eq. (10).

2.2.3. Collisional relaxation

When there exists a difference in velocity between electrons and ions, a collisional drag force acts on both of them in opposite directions each other

$$\vec{F}^\mathrm{C}_\mathrm{ei} = -\vec{F}^\mathrm{C}_\mathrm{ie}.$$

This collisional drag force gives rise to the radial particle flux u_{sr} through Eqs. (4) and (5) and is responsible for the classical collisional transport. In general, the collisional drag force can be written

$$\vec{F}^\mathrm{C}_\mathrm{ei} = -\nu_\mathrm{ei}m_\mathrm{e}n_\mathrm{e}(\vec{u}_\mathrm{e} - \vec{u}_\mathrm{i}).$$

However, this simple definition overestimates the true resistivity of a hydrogen plasma by a factor of two. This overestimation lies in using a usual electron–ion collision frequency ν_ei which was obtained by using a shifted Maxwellian electron distribution function without taking account of electron–electron collisions [22]. The correct results are

$$\nu_{\mathrm{ei}\perp} = \nu_\mathrm{ei} = \frac{Z_\mathrm{i}^2 n_\mathrm{i} e^4 \ln\Lambda_\mathrm{e}}{6\pi(2\pi)^{1/2}\epsilon_0^2 m_\mathrm{e}^{1/2} T_\mathrm{e}^{3/2}}.,$$
$$\nu_{\mathrm{ei}\parallel} = N(Z_\mathrm{eff})\nu_\mathrm{ei},$$

where $N(Z_\mathrm{eff})$ is the correction function of the collisional frequency with respect to the effective charge, which takes account of the effect of electron–electron collisions, and is given in [9]

$$N(Z_\mathrm{eff}) = Z_\mathrm{eff}\frac{1 + 1.198Z_\mathrm{eff} + 0.222Z_\mathrm{eff}^2}{1 + 2.966Z_\mathrm{eff} + 0.753Z_\mathrm{eff}^2},$$

e.g. $N(1) \approx 0.51$ in a plasma for singly charged ions. By defining the collisional frequencies as

$$\nu_\mathrm{ei1} = \frac{B_\theta^2}{B^2}\nu_{\mathrm{ei}\parallel} + \frac{B_\phi^2}{B^2}\nu_{\mathrm{ei}\perp},$$
$$\nu_\mathrm{ei2} = \frac{B_\theta B_\phi}{B^2}(\nu_{\mathrm{ei}\parallel} - \nu_{\mathrm{ei}\perp}),$$
$$\nu_\mathrm{ei3} = \frac{B_\phi^2}{B^2}\nu_{\mathrm{ei}\parallel} + \frac{B_\theta^2}{B^2}\nu_{\mathrm{ei}\perp},$$

the collisional force can be written

$$F^\mathrm{C}_{\mathrm{ei}\theta} = -F^\mathrm{C}_{\mathrm{ie}\theta} = -\nu_\mathrm{ei1}n_\mathrm{e}m_\mathrm{e}(u_{\mathrm{e}\theta} - u_{\mathrm{i}\theta}) - \nu_\mathrm{ei2}n_\mathrm{e}m_\mathrm{e}(u_{\mathrm{e}\phi} - u_{\mathrm{i}\phi}),$$
$$F^\mathrm{C}_{\mathrm{ei}\phi} = -F^\mathrm{C}_{\mathrm{ie}\phi} = -\nu_\mathrm{ei2}n_\mathrm{e}m_\mathrm{e}(u_{\mathrm{e}\theta} - u_{\mathrm{i}\theta}) - \nu_\mathrm{ei3}n_\mathrm{e}m_\mathrm{e}(u_{\mathrm{e}\phi} - u_{\mathrm{i}\phi}).$$

The similar way applies to the electron collisional relaxation with beam ions, giving

$$F^{\mathrm{C}}_{\mathrm{eb}\theta} = -F^{\mathrm{C}}_{\mathrm{be}\theta} = -\nu_{\mathrm{be1}} n_{\mathrm{b}} m_{\mathrm{b}} (u_{\mathrm{e}\theta} - u_{\mathrm{b}\theta}) - \nu_{\mathrm{be2}} n_{\mathrm{b}} m_{\mathrm{b}} (u_{\mathrm{e}\phi} - u_{\mathrm{b}\phi}),$$
$$F^{\mathrm{C}}_{\mathrm{eb}\phi} = -F^{\mathrm{C}}_{\mathrm{be}\phi} = -\nu_{\mathrm{be2}} n_{\mathrm{b}} m_{\mathrm{b}} (u_{\mathrm{e}\theta} - u_{\mathrm{b}\theta}) - \nu_{\mathrm{be3}} n_{\mathrm{b}} m_{\mathrm{b}} (u_{\mathrm{e}\phi} - u_{\mathrm{b}\phi}).$$

Here ν_{be} is given by [8]

$$\nu_{\mathrm{be}} = \frac{n_{\mathrm{e}} Z_{\mathrm{b}}^2 e^4 \ln \Lambda_{\mathrm{e}}}{3\pi (2\pi)^{1/2} \epsilon_0^2 m_{\mathrm{b}} m_{\mathrm{e}}} \left(\frac{m_{\mathrm{e}}}{T_{\mathrm{e}}}\right)^{3/2}, \tag{31}$$

where Z_{b} is the charge of beam ions, and ν_{be1}, ν_{be2} and ν_{be3} are defined in the same manner as ν_{ei}.

The ion collisional drag force with beam ions is simply given by

$$F^{\mathrm{C}}_{\mathrm{ib}\theta} = -F^{\mathrm{C}}_{\mathrm{bi}\theta} = -\nu_{\mathrm{bi}} n_{\mathrm{b}} m_{\mathrm{b}} (u_{\mathrm{i}\theta} - u_{\mathrm{b}\theta}),$$
$$F^{\mathrm{C}}_{\mathrm{ib}\phi} = -F^{\mathrm{C}}_{\mathrm{bi}\phi} = -\nu_{\mathrm{bi}} n_{\mathrm{b}} m_{\mathrm{b}} (u_{\mathrm{i}\phi} - u_{\mathrm{b}\phi}).$$

By estimating the slowing-down time of beam ions in the light of kinetic approach, we obtain [22,23]

$$\nu_{\mathrm{bi}} = \frac{n_{\mathrm{i}} Z_{\mathrm{i}}^2 Z_{\mathrm{b}}^2 e^4 \ln \Lambda_{\mathrm{i}}}{2\pi \epsilon_0^2 m_{\mathrm{b}}} \left(\frac{1}{m_{\mathrm{b}}} + \frac{1}{m_{\mathrm{i}}}\right) \frac{1}{v_{\mathrm{b}} v_{\mathrm{thi}}^2} G\left(\frac{v_{\mathrm{b}}}{v_{\mathrm{thi}}}\right), \tag{32}$$

where v_{thi} is the ion thermal velocity defined by $(2T_{\mathrm{i}}/m_{\mathrm{i}})^{1/2}$ and $\ln \Lambda_{\mathrm{i}}$ the Coulomb logarithm of ion collisions defined by [21]

$$\ln \Lambda_{\mathrm{i}} = 40.3 - \ln \left(\frac{Z_{\mathrm{i}}^2}{T_{\mathrm{i}}} \sqrt{\frac{2 n_{\mathrm{i}} Z_{\mathrm{i}}^2}{T_{\mathrm{i}}}}\right),$$

where the units of n_{i} and T_{i} are the same as those of Eq. (28). G denotes the Chandrasekhar function [24] defined by

$$G(x) \equiv \frac{\mathrm{erf}(x) - x\mathrm{erf}'(x)}{2x^2}, \tag{33}$$

where $\mathrm{erf}(x)$ is the error function and now $x = v_{\mathrm{b}}/v_{\mathrm{thi}}$. Expanding Eq. (33) into power series and expanding it asymptotically provide us with the first term of Eq. (33) as

$$G(x) \approx \frac{2x}{3\pi^{1/2}} \quad (|x| \ll 1),$$
$$G(x) \approx \frac{1}{2x^2} \quad (|x| \gg 1).$$

This function implies that $G(x)$ is inversely proportional to the ion thermal velocity if the beam velocity is sufficiently slower than the ion thermal velocity (i.e. $|x| \ll 1$), while it is inversely proportional to the square velocity of beam ions if it is sufficiently faster than the ion thermal velocity (i.e. $|x| \gg 1$). Putting these dependencies together into the formula Eq. (32), we finally obtain

$$\nu_{\mathrm{bi}} = \frac{n_{\mathrm{i}} Z_{\mathrm{i}}^2 Z_{\mathrm{b}}^2 e^4 \ln \Lambda_{\mathrm{i}}}{4\pi \epsilon_0^2 m_{\mathrm{b}}} \left(\frac{1}{m_{\mathrm{b}}} + \frac{1}{m_{\mathrm{i}}}\right) \frac{1}{v_{\mathrm{b}}^3 + \frac{3\pi^{1/2}}{4} \left(\frac{2T_{\mathrm{i}}}{m_{\mathrm{i}}}\right)^{3/2}}.$$

In analogy with the difference of velocities, a difference of temperatures is forced to relax through collisions to give rise to energy exchange. This energy exchange between electrons and ions is expressed as

$$P^{\mathrm{C}}_{\mathrm{ei}} = -P^{\mathrm{C}}_{\mathrm{ie}} = -\frac{3}{2} \nu_{\mathrm{Tei}} n_{\mathrm{e}} (T_{\mathrm{e}} - T_{\mathrm{i}}),$$

where ν_{Tei} is the electron temperature relaxation frequency with ions (or the equipartition rate) defined by [22]

$$\nu_{\mathrm{Tei}} = \frac{n_{\mathrm{i}} Z_{\mathrm{i}}^2 e^4 \ln \Lambda_{\mathrm{e}}}{3\pi (2\pi)^{1/2} \epsilon_0^2 m_{\mathrm{e}} m_{\mathrm{i}}} \left(\frac{m_{\mathrm{e}}}{T_{\mathrm{e}}}\right)^{3/2}.$$

When a neutral beam is injected in a plasma, the beam particles initially having the injection velocity v_b are rapidly ionized and the resulting beam ions are slowed down by Coulomb collisions . Through the slowing-down process, the beam ions give their energy to electrons and ions of the background plasma and the plasma is then heated. There are two mechanisms to heat the background plasma [9]. One is the beam momentum deposition heating which is proportional to the product of the injected beam momentum and the main ion velocity. The other is the collisional heating through the thermal relaxation due to the Coulomb collisions. The heating powers from NBI are therefore expressed by

$$P_\mathrm{e}^\mathrm{B} = \frac{1}{2} m_\mathrm{b} v_\mathrm{b}^2 \frac{P_\mathrm{b}}{E_\mathrm{b}} [1 - H(v_\mathrm{c})],$$

$$P_\mathrm{i}^\mathrm{B} = m_\mathrm{b} \frac{B_\theta u_{\mathrm{i}\theta} + B_\phi u_{\mathrm{i}\phi}}{B} v_\mathrm{b} \frac{P_{\mathrm{b}\|}}{E_\mathrm{b}} + \frac{1}{2} m_\mathrm{b} v_\mathrm{b}^2 \frac{P_\mathrm{b}}{E_\mathrm{b}} H(v_\mathrm{c}),$$

where $v_\mathrm{c} = (2E_\mathrm{c}/m_\mathrm{b})^{1/2}$ and [12]

$$H(v_\mathrm{c}) = \frac{2}{v_\mathrm{c}^2} \int_0^{v_\mathrm{c}} v dv \frac{v_\mathrm{c}^3}{v^3 + v_\mathrm{c}^3}, = \frac{2}{v_\mathrm{c}^2} \left[\frac{1}{6} \ln \frac{1 - v_\mathrm{c} + v_\mathrm{c}^2}{1 + 2v_\mathrm{c} + v_\mathrm{c}^2} + \frac{1}{3^{1/2}} \left(\frac{\pi}{6} + \tan^{-1} \frac{2v_\mathrm{c} - 1}{3^{1/2}} \right) \right].$$

2.2.4. Neoclassical viscosity

The neoclassical transport results from the Coulomb collision and the inhomogeneity of the toroidal magnetic field, so that in an axisymmetric system poloidal rotation of the plasma is damped by a parallel viscous force [9].

In order to evaluate the neoclassical viscosity, we have incorporated the NCLASS module [25,26] into the TASK/TX code. The NCLASS module provides the neoclassical quantities such as resistivity, bootstrap current and viscosity on a magnetic surface, and is applicable to a multi-species axisymmetric plasma of arbitrary aspect ratio. We therefore use the approximate form of the neoclassical viscous force:

$$F_{s\theta}^\mathrm{NC} \equiv -n_s m_s \nu_{\mathrm{NC}s} u_{s\theta} = -\frac{\langle B^2 \rangle \hat{\mu}_{11}^{si}}{n_s m_s B_\theta^2} n_s m_s u_{s\theta},$$

where $\nu_{\mathrm{NC}s}$ denotes the neoclassical poloidal viscosity and $\hat{\mu}_{11}^{si}$ is the normalized viscosity coefficient which is given by Eq. (15) in Ref. [25], and is in the output from the NCLASS module. Here, s appeared in $\hat{\mu}_{11}^{si}$ denotes the particle species and i the charge state. Since we only consider the momentum flux in the present analyses, we only use the viscosity $\hat{\mu}_{11}^{si}$ for the poloidal flow in the momentum viscous stress and we neglect the viscosities associated with the heat flux.

In using the NCLASS module, we have adopted the simple formula of the trapped particle fraction f_t [27]

$$f_t = 1.46\epsilon^{1/2} - 0.46\epsilon^{3/2}. \tag{34}$$

The neoclassical transport effect induced by this viscous force will be discussed in Section 2.3. The fact that $F_{s\theta}^\mathrm{NC}$ acting on electrons and ions are not of the same magnitude implies that the neoclassical induced transport seems non-ambipolar. On the longer time scale of the toroidal angular momentum damping time, however, the toroidal angular momentum damps to a certain value, determining the asymptotic ambipolar transport in terms of the pressure gradient [4].

2.2.5. Forces induced by turbulent fluctuations

We assume that turbulent fluctuations arising in a plasma are absorbed somewhere in a plasma and momentum and energy are conserved. If the fluctuations do not propagate radially, the poloidal momentum is transferred from electrons to ions or vice versa. By virtue of the poloidal momentum conservation, however, the reaction force on electrons $F_{\mathrm{e}\theta}^\mathrm{W}$ should have the same magnitude of and the opposite direction to $F_{\mathrm{i}\theta}^\mathrm{W}$ on ions. This implies that the transport induced by this force is the same for electrons and ions, that is, intrinsically ambipolar [28]. On the other hand, if the fluctuations do propagate radially, they may act as a perpendicular viscosity. Since appropriate theory to describe the wave-particle interaction through fluctuations has not been established, so that we introduce a model formula as is described in the following.

We assume that anomalous particle transport results from the poloidal momentum exchange between electrons and ions mediated by the turbulent electric field. The resulting force can be generally written as

$$\vec{F}_s^{\mathrm{W}} = e_s\langle\tilde{n}\tilde{\vec{E}} + n\tilde{\vec{V}} \times \tilde{\vec{B}}\rangle.$$

In the case of the electrostatic fluctuation, the force acting on electrons can be expresses as [29,30]

$$F_{\mathrm{e}\theta}^{\mathrm{W}} = eB_\phi n_{\mathrm{e}} D_{\mathrm{e}}\left[-\frac{1}{n_{\mathrm{e}}}\frac{\mathrm{d}n_{\mathrm{e}}}{\mathrm{d}r} + \frac{e}{T_{\mathrm{e}}}E_r - \left\langle\frac{\omega}{m}\right\rangle_{\mathrm{e}} r\frac{eB_\phi}{T_{\mathrm{e}}} - \left(\frac{\mu_e}{D_{\mathrm{e}}} - \frac{1}{2}\right)\frac{1}{T_{\mathrm{e}}}\frac{\mathrm{d}T_{\mathrm{e}}}{\mathrm{d}r}\right], \tag{35}$$

where ω and m are the mode frequency and poloidal mode number respectively, and $\langle\omega/m\rangle_{\mathrm{e}}r$ denotes the spectrum average of the phase velocity in the poloidal direction. In the above expression, we have assumed a symmetric wave spectrum with respect to $k_\parallel$ and weak velocity shear. The factor D_{e} is proportional to the square of the wave amplitude and corresponds to the ordinary diffusion coefficient. If the Lorentz force $en_{\mathrm{e}}u_{\mathrm{e}r}B_\phi$ balances with this force, the particle flux should include the term $-D_{\mathrm{e}}(\mathrm{d}n_{\mathrm{e}}/\mathrm{d}r)$ and thus particles diffuse radially. Although it is possible to consider a force related to the ion motion and D_{i}, it is hard to describe the particle diffusion through the model formula because the ion pressure gradient almost balances with the radial electric field. We then concentrate on the form of Eq. (35) in the present analyses.

Since we can approximately express the terms in the angled bracket in Eq. (35) using $u_{\mathrm{e}\perp}$, we adopt model formulae

$$F_{\mathrm{e}\theta}^{\mathrm{W}} = -F_{\mathrm{i}\theta}^{\mathrm{W}} = -\frac{e^2B_\phi^2D_{\mathrm{e}}}{T_{\mathrm{e}}}n_{\mathrm{e}}\left(u_{\mathrm{e}\theta} - \frac{B_\theta}{B_\phi}u_{\mathrm{e}\phi} - \left\langle\frac{\omega}{m}\right\rangle_{\mathrm{e}} r\right), \tag{36}$$

$$F_{\mathrm{e}\phi}^{\mathrm{W}} = -F_{\mathrm{i}\phi}^{\mathrm{W}} = \frac{e^2B_\phi^2D_{\mathrm{e}}}{T_{\mathrm{e}}}\frac{B_\theta}{B_\phi}n_{\mathrm{e}}\left(u_{\mathrm{e}\theta} - \frac{B_\theta}{B_\phi}u_{\mathrm{e}\phi} - \left\langle\frac{\omega}{m}\right\rangle_{\mathrm{i}} r\right), \tag{37}$$

where the first two terms in parentheses comprise the perpendicular velocity of electrons. We take not only $F_{\mathrm{e}\theta}^{\mathrm{W}}$ but also $F_{\mathrm{e}\phi}^{\mathrm{W}}$ into account. By adding $F_{\mathrm{e}\phi}^{\mathrm{W}}$ in the toroidal momentum equation, we can express the fluctuation induced force as a perpendicular force. Since it is assumed that parallel force vanishes, no current is driven in the parallel direction. In the present analyses, we assume that the spectrum averaged phase velocity vanishes, i.e., $\langle\omega/m\rangle_{\mathrm{e,i}}r = 0$.

The perpendicular viscosity μ_s is governed by the turbulence because the collisional part of the perpendicular viscosity is very small. The turbulent viscosity results from the radial propagation of the fluctuation. Since the viscous force on electrons and ions are not always of the same magnitude, the transport due to the viscosity is therefore non-ambipolar; the particle flux is proportional to $\partial^3p/\partial r^3$. We usually assume that μ_s has the same radial profile as that of thermal diffusivity χ_s.

2.2.6. Transport of neutrals

Since there exist a number of groups of neutrals having different energies in a plasma, the Monte Carlo method is often used to describe the transport of neutrals. We now employ, however, the simple diffusion equations Eq. (10) for two groups of neutrals to describe the behavior of neutrals semi-quantitatively. One group includes slow neutrals generated by gas puff or recycling with wall temperature, while fast neutrals are generated by charge exchange and NB injection with ion temperature.

We opt for the following formulae for the diffusion coefficients of neutrals

$$D_{01} = \frac{v_0^2}{\nu_{11} + \nu_{12} + \nu_{1\mathrm{i}}},$$

$$D_{02} = \frac{v_{\mathrm{thi}}^2}{\nu_{21} + \nu_{22} + \nu_{2\mathrm{i}}},$$

where the subscript 1 denotes the slow (thermal) neutrals and 2 the fast neutrals, $\nu_{11} = n_{01}\langle\sigma_{00}v_0\rangle$ is the collision frequency between slow neutrals, $\nu_{1\mathrm{i}} = \nu_{2\mathrm{i}} = n_{\mathrm{i}}\langle\sigma_{0\mathrm{i}}v_{\mathrm{thi}}\rangle$ between neutrals and ions, $\nu_{21} = n_{01}\langle\sigma_{00}v_{\mathrm{thi}}\rangle$ between slow neutrals and fast neutrals and $\nu_{12} = \nu_{22} = n_{02}\langle\sigma_{00}v_{\mathrm{thi}}\rangle$ between fast neutrals. We choose a typical velocity of slow neutrals $v_0 \sim 1.5 \times 10^3$ m/s and a typical collisional cross section $\sigma_{00} \sim \sigma_{0\mathrm{i}} \sim 8.8 \times 10^{-21}$ m^2 [21].

2.2.7. Radiation loss

A plasma emits electromagnetic radiation when the charged particles are microscopically accelerated. Owing to their lighter mass, the electrons experience larger acceleration than the ions. Consequently they radiate much more strongly, so that all we have to consider is the radiation of the electrons.

The electrons are accelerated through collisional processes and thus emit the radiation called bremsstrahlung. They are also subject to the acceleration of their cyclotron motion and the resulting radiation is called cyclotron or synchrotron radiation. The power loss due to the cyclotron radiation is, however, usually much smaller than bremsstrahlung in a D–T fusion plasma [10]. According to Ref. [10], the power due to bremsstrahlung is written as

$$P_{\rm i}^{\rm R} = g\frac{e^6}{6(3/2)^{1/2}\pi^{3/2}\epsilon_0^3 c^3 h m_{\rm e}^{3/2}} Z_{\rm i}^2 n_{\rm e} n_{\rm i} T_{\rm e}^{1/2},$$

where g is the Gaunt factor and $g \simeq 2(3)^{1/2}/\pi$ is given in our case and h is the Planck's constant.

In the presence of impurities, we should consider further losses due to the atomic processes of line radiation and recombination radiation, but now the impurity effect is outside of our scope of the present analysis and we therefore ignore it.

2.3. Stationary flux

Before completing the description of our physical model, we discuss the physical mechanism described in our model by considering a stationary flux solution for electrons by setting the inertial terms in Eqs. (3)–(5) to zero. Neglecting the perpendicular viscosity μ_s and relatively smaller centrifugal force, after a lengthy algebraic calculation we obtain the radial and toroidal velocities for electrons as follows:

$$\begin{aligned} u_{\rm er} = & -\frac{1}{(1+\alpha)\bar{\nu}_3}\frac{\bar{\nu}_3(\bar{\nu}_1+\nu_{\rm NCe})-\bar{\nu}_2^2}{n_{\rm e}m_{\rm e}\Omega_{{\rm e}\phi}^2}\frac{\partial p}{\partial r} + \frac{1}{(1+\alpha)\bar{\nu}_3\Omega_{{\rm e}\phi}}\frac{e}{m_{\rm e}}\left(-\hat{\nu}_\alpha E_\phi + \hat{\nu}_\beta E_\theta\right) \\ & + \frac{1}{(1+\alpha)\bar{\nu}_3}\frac{1}{n_{\rm e}m_{\rm e}\Omega_{{\rm e}\phi}}\left(\hat{\nu}_\alpha F_{{\rm e}\phi}^{\rm W} + \hat{\nu}_\beta F_{{\rm e}\theta}^{\rm W}\right) \\ & + \frac{1}{(1+\alpha)\bar{\nu}_3\Omega_{{\rm e}\phi}}\left[(\hat{\nu}_\alpha\nu_{\rm eb3} - \hat{\nu}_\beta\nu_{\rm eb2})u_{{\rm b}\phi} + \{(\nu_{\rm ei3}-\bar{\nu}_3)\hat{\nu}_\alpha + \nu_{\rm eb2}\hat{\nu}_\beta\}u_{{\rm i}\phi}\right] \\ & + \frac{1}{(1+\alpha)\bar{\nu}_3\Omega_{{\rm e}\phi}}\left[(\hat{\nu}_\alpha\nu_{\rm eb2} - \hat{\nu}_\beta\nu_{\rm eb1})u_{{\rm b}\theta} + \{-\nu_{\rm eb2}\hat{\nu}_\alpha + (\bar{\nu}_1+\nu_{\rm NCe}-\nu_{\rm ei1})\hat{\nu}_\beta\}u_{{\rm i}\theta}\right], \end{aligned} \tag{38}$$

$$\begin{aligned} u_{{\rm e}\phi} = & \frac{1}{(1+\alpha)\bar{\nu}_3}\frac{\hat{\nu}_\alpha}{n_{\rm e}m_{\rm e}\Omega_{{\rm e}\phi}}\frac{\partial p}{\partial r} - \frac{1}{(1+\alpha)\bar{\nu}_3}\frac{e}{m_{\rm e}}\left(E_\phi + \frac{B_\theta}{B_\phi}E_\theta\right) \\ & + \frac{1}{(1+\alpha)\bar{\nu}_3}\frac{1}{n_{\rm e}m_{\rm e}}\left(F_{{\rm e}\phi}^{\rm W} - \frac{B_\theta}{B_\phi}F_{{\rm e}\theta}^{\rm W}\right) \\ & + \frac{1}{(1+\alpha)\bar{\nu}_3}\left[\left(\nu_{\rm eb3} + \nu_{\rm eb2}\frac{B_\theta}{B_\phi}\right)u_{{\rm b}\phi} + \left(\nu_{\rm ei3} + \nu_{\rm ei2}\frac{B_\theta}{B_\phi} + \hat{\nu}_\alpha\frac{B_\theta}{B_\phi}\right)u_{{\rm i}\phi}\right] \\ & + \frac{1}{(1+\alpha)\bar{\nu}_3}\left[\left(\nu_{\rm eb2} + \nu_{\rm eb1}\frac{B_\theta}{B_\phi}\right)u_{{\rm b}\theta} - \left\{(\bar{\nu}_1+\nu_{\rm NCe}-\nu_{\rm ei1})\frac{B_\theta}{B_\phi} - \nu_{\rm eb2}\right\}u_{{\rm i}\theta}\right] \end{aligned} \tag{39}$$

where

$$\bar{\nu}_1 \equiv \nu_{\rm ei1} + \nu_{\rm eb1} + \nu_{\rm L} + \nu_{0{\rm e}}, \quad \bar{\nu}_2 \equiv \nu_{\rm ei2} + \nu_{\rm eb2}, \quad \bar{\nu}_3 \equiv \nu_{\rm ei3} + \nu_{\rm eb3} + \nu_{\rm L} + \nu_{0{\rm e}},$$

$$\hat{\nu}_\alpha \equiv \bar{\nu}_2 + (\bar{\nu}_1 + \nu_{\rm NCe})\frac{B_\theta}{B_\phi}, \quad \hat{\nu}_\beta \equiv \bar{\nu}_3 + \bar{\nu}_2\frac{B_\theta}{B_\phi},$$

$$\alpha \equiv \frac{\bar{\nu}_1 + \nu_{\rm NCe}}{\bar{\nu}_3}\frac{B_\theta^2}{B_\phi^2} + 2\frac{\bar{\nu}_2}{\bar{\nu}_3}\frac{B_\theta}{B_\phi}, \quad \Omega_{{\rm e}\phi} \equiv \frac{eB_\phi}{m_{\rm e}}, \quad \text{and} \quad \nu_{\rm eb} \equiv \frac{n_{\rm b}m_{\rm b}}{n_{\rm e}m_{\rm e}}\nu_{\rm be}.$$

Here, $p = p_{\rm e} + p_{\rm i}$ denotes the total pressure. The neoclassical viscosity acts as the damping rate and α means its contribution to the parallel direction. The poloidal velocity formula can also be derived in a similar manner.

The first four terms on the right-hand side of Eq. (38) represent the neoclassical diffusion, Ware pinch, turbulent diffusion and neoclassical pinch caused by the momentum input from NBI respectively. The last term is a negligible contribution from the poloidal rotation of ions. In Eq. (39), the first three terms represent the bootstrap current, neoclassical resistivity and turbulent-induced current, respectively. The last two terms are also small contributions from the rotation of bulk ions. In order to evaluate the parallel resistivity, we combine the second term of the right hand side of Eq. (39) with corresponding term in ion poloidal velocity equation to obtain

$$\eta_{\parallel} = \frac{m_e(1+\alpha)\bar{\nu}_3}{n_e e^2}\frac{B_\phi^2}{B^2}, \tag{40}$$

and it is used for estimating ohmic current. In the limit of $B_\theta \to 0$, we recover the Spitzer resistivity, $N(Z_{\mathrm{eff}})m_e\nu_{ei}/n_e e^2$.

We remark that the major neoclassical effects such as the spatial diffusion, Ware pinch, resistivity and bootstrap current are all included in our model. We also note that the neoclassical effect on the turbulent transport is included as well.

Since the neoclassical viscosity strongly suppresses the poloidal rotation of ions, $u_{i\theta}$ is small in the core region. When NBI is turned on, electrons are subject to a collisional drag force from beam ions and the radial particle flux begins to be generated. This beam-induced flux, the fifth term in Eq. (38), is directed outward in co-injection case and inward in counter-injection case. A reduction of the particle flux due to the toroidal rotation of ions is usually small, because the bulk ion velocity is much smaller than the beam ion velocity. This toroidal rotation in turn contributes to the modification of the radial electric field. According to the radial force balance equation of ions Eq. (3) in a steady state, we obtain

$$E_r = -u_{i\theta}B_\phi + u_{i\phi}B_\theta + \frac{1}{Z_i e n_i}\frac{\partial p_i}{\partial r},$$

and this relation points out that E_r is expected to increase for co-NBI and to decrease for counter-NBI.

2.4. Boundary conditions

When we solve the set of 20 equations, Eqs. (2)–(10) and (16)–(20), appropriate boundary conditions should be imposed on them. Since the set of equations consists of 11 second-order differential equations and four first-order differential equations, we need a total of 26 boundary conditions to solve them. They are determined in the following.

On the magnetic axis, $r = 0$, we set half the number of boundary conditions as

$$\frac{\partial \Phi}{\partial r} = 0, \quad r\dot{A}_\theta = 0, \quad \frac{\partial \dot{A}_\phi}{\partial r} = 0, \quad rn_s u_{sr} = 0, \quad rn_s u_{s\theta} = 0,$$
$$\frac{\partial n_s u_{s\phi}}{\partial r} = 0, \quad \frac{\partial n_s T_s}{\partial r} = 0 \quad \text{and} \quad \frac{\partial n_{0s}}{\partial r} = 0,$$

while on the wall surface, $r = b$, other half as

$$\Phi = 0, \quad \frac{\partial r\dot{A}_\theta}{\partial r} = rB_{\phi V}, \quad \frac{\partial A_\phi}{\partial r} = -B_{\theta b}, \quad rn_s u_{sr} = 0, \quad rn_s u_{s\theta} = 0,$$
$$n_s u_{s\phi} = 0, \quad \frac{\partial n_s T_s}{\partial r} = 0, \quad \frac{\partial n_{01}}{\partial r} = \frac{\Gamma_0}{D_{01}}, \quad \text{and} \quad n_{02} = 0,$$

where $B_{\phi V}$ is the vacuum toroidal magnetic field, $B_{\theta b}$ the poloidal magnetic field on the wall surface defined by the plasma current as $B_{\theta b} = \mu_0 I_p/2\pi b$, D_{01} the particle diffusivity for neutral density n_{01}, Γ_0 the particle influx from the wall, which is typically determined by gas-puffing. Since Φ is the electrostatic potential and reference potential has an arbitrariness, we set it on the wall to zero. We assume that the adhesion condition always holds in the very vicinity of the wall, setting the toroidal and poloidal rotations to zero.

2.5. Initial conditions

Initial conditions more or less govern a simulation result in this sort of self-consistent nonlinear simulations. What is needed for initial conditions is that the number of externally-given initial conditions should be reduced as few as possible and the other conditions are consistently constructed from the given conditions. Another important point is that all the dependent variables and their derivatives satisfy the continuity condition everywhere in the calculation domain. In general, variables in the core behave differently from those in the SOL. At the plasma surface, however, they must be continuously connected between two regions because the Galerkin method requires continuity of dependent variables, and in addition continuity of their derivatives should be satisfied in the light of numerical stability. We therefore set the initial conditions for seven variables to satisfy the above conditions as

$$n_s(r) = \begin{cases} (n_{s0} - n_{sa})\left[1 - (r/a)^3\right] + n_{sa} & (0 \leqslant r \leqslant a), \\ n_{sa} + \sum\limits_{i=1}^{4} a_{ni}(r-a)^i & (a \leqslant r \leqslant b), \end{cases}$$

$$p_s(r) = \begin{cases} n_s(r)\left[(T_{s0} - T_{sa})\left\{1 - (r/a)^2\right\}^2 + T_{sa}\right] & (0 \leqslant r \leqslant a), \\ p_{sa} + \sum\limits_{i=1}^{4} a_{pi}(r-a)^i & (a \leqslant r \leqslant b), \end{cases}$$

$$n_{01}(r) = n_{01\mathrm{init}},$$

$$B_\phi(r) = B_{\phi V},$$

$$B_\theta(r) = \begin{cases} \frac{\mu_0 I_\mathrm{p}}{2\pi r}\left[1 - \{1 - (r/a)^2\}^3\right] & (0 \leqslant r \leqslant a), \\ \frac{\mu_0 I_\mathrm{p}}{2\pi r} & (a \leqslant r \leqslant b), \end{cases}$$

where n_{s0} is the density on the magnetic axis, n_{sa} the density at the plasma surface, n_{sb} the density on the wall, the same goes for the temperature T_s and $n_{01\mathrm{init}}$ the initial constant density of slow neutrals. Here, the coefficients a_{ni} and a_{pi} for the density and the pressure profiles are determined by the conditions: $n_s(a) = n_{sa}$, $n''_s(a) = 0$, $n_s(b) = n_{sb}$, $n'_s(b) = 0$, $p_s(a) = p_{sa}$, $p''_s(a) = 0$, $p_s(b) = p_{sb}$, and $p'_s(b) = 0$.

Using these defined variables, we build up remaining variables. First, we can readily calculate the electron toroidal velocity and toroidal electromagnetic potential by analytically integrating and differentiating the poloidal magnetic field, respectively, to obtain

$$n_\mathrm{e} u_{\mathrm{e}\phi}(r) = \begin{cases} -\frac{1}{e\mu_0 r}\frac{\partial}{\partial r}(rB_\theta) = -\frac{3I_\mathrm{p}}{\pi a^2}\left[1 - (r/a)^2\right]^2 & (0 \leqslant r \leqslant a), \\ 0 & (a \leqslant r \leqslant b), \end{cases} \tag{41}$$

$$A_\phi(r) = \begin{cases} -\int_0^r B_\theta \,\mathrm{d}r = -\frac{\mu_0 I_\mathrm{p} r^2}{24\pi a^6}(2r^4 - 9a^2r^2 + 18a^4) & (0 \leqslant r \leqslant a), \\ -\int_0^a B_\theta \,\mathrm{d}r - \int_a^r B_\theta \,\mathrm{d}r = -\frac{11\mu_0 I_\mathrm{p}}{24\pi} - \frac{\mu_0 I_\mathrm{p}}{2\pi}(\ln r - \ln a) & (a \leqslant r \leqslant b). \end{cases} \tag{42}$$

The relation of Eq. (41) can be derived from Eq. (13) by neglecting the displacement current (time-derivative term) and the ion current, and Eq. (42) comes from Eq. (21).

Next we focus on the major force balance relations of both radial and poloidal velocities, Eqs. (3) and (4) in a steady state. In the toroidal component of the equation of motion for electrons, toroidal electron velocity is balanced among the toroidal electric field and $\vec{v} \times \vec{B}$ force,

$$-\frac{e}{m_\mathrm{e}} n_\mathrm{e} E_\phi - \frac{e}{m_\mathrm{e}} B_\theta n_\mathrm{e} u_{\mathrm{e}r} - \nu_{\mathrm{ei}3} n_\mathrm{e} u_{\mathrm{e}\phi} = 0. \tag{43}$$

Neoclassical force is usually as strong as the $\vec{v} \times \vec{B}$ force in the poloidal equation of motion for both electrons and ions,

$$\frac{e}{m_\mathrm{e}}B_\phi n_\mathrm{e}u_{\mathrm{e}r} - \nu_\mathrm{NCe}n_\mathrm{e}u_{\mathrm{e}\theta} = 0, \tag{44}$$

$$-Z_\mathrm{i}\frac{e}{m_\mathrm{i}}B_\phi n_\mathrm{i}u_{\mathrm{i}r} - \nu_\mathrm{NCi}n_\mathrm{i}u_{\mathrm{i}\theta} = 0. \tag{45}$$

The radial electric field is mainly governed by the ion pressure gradient, but the ion poloidal velocity is not too small to be negligible. On the other hand, the radial force balance among the pressure gradient, the radial electric field and the $\vec{v}\times\vec{B}$ force

$$-\frac{1}{m_\mathrm{e}}\frac{\partial(n_\mathrm{e}T_\mathrm{e})}{\partial r} - \frac{e}{m_\mathrm{e}}n_\mathrm{e}E_r - \frac{e}{m_\mathrm{e}}B_\phi n_\mathrm{e}u_{\mathrm{e}\theta} + \frac{e}{m_\mathrm{e}}B_\theta n_\mathrm{e}u_{\mathrm{e}\phi} = 0, \tag{46}$$

$$-\frac{1}{m_\mathrm{i}}\frac{\partial(n_\mathrm{i}T_\mathrm{i})}{\partial r} + Z_\mathrm{i}\frac{e}{m_\mathrm{i}}n_\mathrm{i}E_r + Z_\mathrm{i}\frac{e}{m_\mathrm{i}}B_\phi n_\mathrm{i}u_{\mathrm{i}\theta} = 0, \tag{47}$$

determines the poloidal velocity for electrons and ions. By solving Eqs. (43)–(47) simultaneously and assuming the condition $n_\mathrm{e}u_{\mathrm{e}r} = n_\mathrm{i}u_{\mathrm{i}r}$, we can obtain the initial profiles of E_r, E_ϕ, $n_s u_{sr}$ and $n_s u_{s\theta}$. The first two quantities, E_r and E_ϕ, give Φ and $\dot{A}_\theta$, respectively.

Finally, we numerically integrate Eqs. (12) and (21) in a steady state to obtain

$$\Phi(r) = -\int_0^r E_r\,\mathrm{d}r,$$

$$rA_\theta(r) = \int_0^r rB_\phi\,\mathrm{d}r = -\mu_0\int_0^r r\left(\int_0^r \sum_{s=e,i} e_s n_s u_{s\theta}\mathrm{d}r\right)\mathrm{d}r.$$

It is reasonable to set the remainder of the variables to zero in an initial state because $E_\theta\ (= -\dot{A}_\phi)$, $n_\mathrm{i}u_{\mathrm{i}\phi}$, n_{02} and beam components are very small compared with the other variables.

3. Numerical methods

3.1. Transformation of the coordinate system

As discussed in Section 2.4, for some variables natural boundary conditions should be imposed on the magnetic axis. Natural boundary conditions can be usually applied by integrating a diffusive term by parts. In the cylindrical coordinates, however, the boundary terms resulting from integration by parts consist of the product with the radial coordinate variable r, so that we have difficulty in imposing the natural boundary condition of the variable on the axis because its gradient cannot be determined uniquely at $r = 0$.

As an example, we consider a simple diffusion equation in a cylindrical system

$$0 = \frac{1}{r}\frac{\partial}{\partial r}\left(rD\frac{\partial f}{\partial r}\right) + S, \tag{48}$$

where f is the dependent variable, D the diffusivity and S the source term. In deriving the weak form of Eq. (48), we multiply it with a weight function $w(r)$ and integrate over the volume of the cylinder with unit axial length

$$0 = 2\pi\int_0^a\left[\frac{\partial}{\partial r}\left(rD\frac{\partial f}{\partial r}\right) + rS\right]w\,\mathrm{d}r.$$

Then we carry out integration by parts to obtain

$$0 = 2\pi\left[rD\frac{\partial f}{\partial r}w\right]_0^a - 2\pi\int_0^a rD\frac{\partial f}{\partial r}\frac{\partial w}{\partial r}\,\mathrm{d}r + 2\pi\int_0^a rSw\,\mathrm{d}r.$$

Even if we want to impose the natural boundary condition of $\partial f/\partial r = 0$ at $r = 0$, the gradient has an arbitrary value because the boundary term is always nought on the axis due to $r = 0$. This leads to a numerical instability near the axis and we cannot always obtain a correct result.

To avoid the indefiniteness of the gradient on the axis, we introduce the new radial coordinate, s, defined by $s = r^2$. With this coordinate, the natural boundary condition at $r = 0$ can be automatically satisfied because the r-derivative is a product of r and the s-derivative, i.e.

$$\left.\frac{\partial f}{\partial r}\right|_{r=0} = 2r\left.\frac{\partial f}{\partial s}\right|_{r=0} = 0. \tag{49}$$

We transform Eq. (48) to the one in s coordinate, then we obtain

$$0 = 4\frac{\partial}{\partial s}\left(sD\frac{\partial f}{\partial s}\right) + S.$$

Note that f, D and S are now the functions of s. Using a weak form of the set of equations and integrating by parts allows us to obtain

$$0 = 4\pi\left[sD\frac{\partial f}{\partial s}w\right]_0^{a^2} - 4\pi\int_0^{a^2} sD\frac{\partial f}{\partial s}\frac{\partial w}{\partial s}\,\mathrm{d}s + \pi\int_0^{a^2} Sw\,\mathrm{d}s. \tag{50}$$

Note that w is also a function of s and the integral domain is changed to $(0, a^2)$.

3.2. Choice of dependent variables

Before solving the set of nonlinear equations numerically, it is very important to define a dependent variable in each equation. In developing the TASK/TX code, we adopt the Galerkin method as a numerical tool to solve a radial profile of a variable. As will be described in Section 3.4, a linear interpolation function is used as the finite element approximation function. That is to say, dependent variables and coefficients are represented as a linear function in an element. As described in the preceding section, independent variable of the radial coordinate is not r but s. When we think of the boundary conditions discussed in Section 2.4, some variables such as $n_s u_{sr}$ and $n_s u_{s\theta}$ are set to zero on axis and these kinds of variables essentially behave like a linear function in r coordinate near the axis. When we interpolate them using a linear interpolation function in s coordinate, they have the dependence on $s^{1/2}$ and the accuracy of approximation is strongly deteriorated near the axis because a square root function cannot be suitably expressed by not only the linear function but also the higher-order Lagrange function. To avoid this problem, we multiply these variables by r and define the resulting variables as the dependent variables in our calculation. They are summarized in Table 1.

3.3. Discretization of the domain

Near the plasma surface, some physical quantities such as the radial electric field, the plasma densities and the toroidal velocities may vary substantially. We are interested in phenomena which occur near the plasma surface: the L–H transition and the formation of the edge transport barrier. To analyze the plasma behavior near the plasma surface accurately, we need to accumulate the spatial mesh in the vicinity of the plasma surface.

In our simulation, the radial mesh should satisfy the condition that one of the grid points should be on the plasma surface. In order to generate a radial mesh suitable for our simulation, we construct it in the following way. First, we consider a Lorentzian function in the following form:

$$f(r) = C_0\left[1 + \frac{C_1}{1 + \{(r - r_s)/w\}^2}\right], \tag{51}$$

Table 1
The dependent variables in the TASK/TX code

Maxwell's equations	Φ, $r\dot{A}_\theta$, $\dot{A}_\phi$, A_ϕ, rA_θ
Equations for bulk species	n_s, $rn_s u_{sr}$, $rn_s u_{s\theta}$, $n_s u_{s\phi}$, $n_s T_s$
Equations for beam ions	n_b, $rn_\mathrm{b} u_{\mathrm{b}\theta}$, $n_\mathrm{b} u_{\mathrm{b}\phi}$
Equations for neutrals	n_{01}, n_{02}

where C_0 is a normalization constant, C_1 the amplitude of a peak, r_s the center position of the peak and w the width of the peak. The Lorentzian function $f(r)$ has a peak at $r = r_s$ and the magnitude of the peak can be controlled by varying C_1 and w. We then integrate $f(r)$ from 0 to r to obtain

$$F(r) = \int_0^r f(r')\mathrm{d}r' = C_0\left[r + C_1\left\{w\arctan\left(\frac{r - r_s}{w}\right)\right\} + w\arctan\left(\frac{r_s}{w}\right)\right].$$

The resultant function $F(r)$ is close to a linear function except near $r = r_s$ where the gradient of $F(r)$ becomes large. When we give the equally spaced mesh of F, calculating the inverse function of $r = r(F)$ and mapping from the original r coordinate to the generated coordinate allow us to obtain the appropriate r mesh which has fine grids near $r = r_s$.

The way to construct the mesh so far, however, does not always satisfy the condition that the plasma surface lies just on the grid point. We therefore take the following algorithm:

(1) As a trial, we generate a mesh in the above way using the given C_1, r_s and w.
(2) Unless the plasma surface is on the grid, we choose the radial grid position nearest to the plasma surface and obtain the grid position in the original coordinate (i.e. the coordinate before mapping) corresponding to the grid position in the generated coordinate.
(3) C_1 is then calibrated to match the position in the generated mesh corresponding to the position obtained above with the plasma surface exactly.

As an example, we show a radial mesh with the condition of $N_{\max} = 60$, $a = 0.35$, $b = 0.4$, $C_1 = 10$, $r_s = a$ and $w = 0.05$, where $N_{\max}$ is the total number of mesh points. We also prepare the original radial coordinate whose domain is $(0, b)$ and is equally separated into sixty elements. After the generation of the new coordinate, it is found that $r \simeq 0.3514$ is the nearest grid to the plasma surface of $r_s = 0.35$ and corresponds to $r_{\mathrm{org}} = 0.2867$ in the original coordinate. The C_1 value which makes the plasma surface set just on the grid after mapping is provided as $C_1 \simeq 8.016$. Finally by using the new C_1 instead of the old one, we obtain a new radial mesh satisfying our requirement by regenerating it in the same way. In Fig. 1, we show the spatial mesh in r and $s = r^2$ coordinates usually used in our simulation.

3.4. Algorithm for solving the nonlinear evolution equations

Using the generated radial mesh in the preceding section, we use the Galerkin method as the finite element method to solve the set of equations, Eqs. (2)–(9) and (16)–(20) . The interpolation function we use is linear. We adopt the decoupled formulation, which means that the interpolation function depends on the spatial coordinate only and the nodal values, viz. variables, are functions of time t only.

Let us consider the time advancing scheme for a general time-dependent nonlinear equation

$$\frac{\mathrm{d}\vec{u}}{\mathrm{d}t} = \overleftrightarrow{C}(\vec{u}) \cdot \vec{u} + \vec{R}(\vec{u}),$$

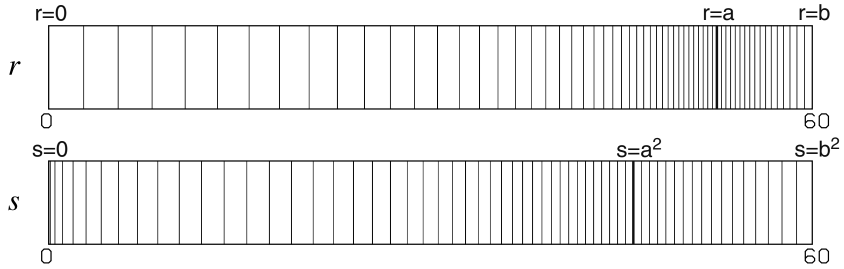

Fig. 1. The generated r and s mesh points in the case of $C_1 \simeq 8.016$, $r_s = a = 0.35$ and $w = 0.05$. The total number of elements $N_{\max}$ is 60. $r = 0$ denotes the magnetic axis, a the plasma surface radius and b the wall radius.

where $\vec{u}$ is a dependent variable of time t and space, $\overleftrightarrow{C}$ is a coefficient matrix of $\vec{u}$ depending on $\vec{u}$ and $\vec{R}$ is a source term. Applying the finite difference approximation to the time derivative reduces the equation to

$$\frac{\vec{u}_{n+1}-\vec{u}_n}{\Delta t}=(1-\alpha)\left[\overleftrightarrow{C}(\vec{u}_n)\cdot\vec{u}_n+\vec{R}(\vec{u}_n)\right]+\alpha\left[\overleftrightarrow{C}(\vec{u}_{n+1})\cdot\vec{u}_{n+1}+\vec{R}(\vec{u}_{n+1})\right], \tag{52}$$

where the subscript n denotes the nth number of time defined by $t=n\Delta t$ with a time step Δt and α is an arbitrary number of $0\leqslant\alpha\leqslant 1$. The full-implicit method of $\alpha=1$ has the advantage of numerical robustness and allows us to use larger time steps in comparison with the explicit method.

After a short algebraic calculation, we rewrite Eq. (52) in the following form

$$\overleftrightarrow{M}(\vec{u}_{n+1})\cdot\vec{u}_{n+1}=\vec{F}(\vec{u}_{n+1})+\vec{G}(\vec{u}_n), \tag{53}$$

where

$$\begin{aligned}
&\overleftrightarrow{M}(\vec{u}_{n+1})\equiv\overleftrightarrow{I}-\alpha\Delta t\,\overleftrightarrow{C}(\vec{u}_{n+1}),\\
&\vec{F}(\vec{u}_{n+1})\equiv\alpha\Delta t\vec{R}(\vec{u}_{n+1}),\\
&\vec{G}(\vec{u}_n)\equiv\vec{u}_n+(1-\alpha)\Delta t[\overleftrightarrow{C}(\vec{u}_n)\cdot\vec{u}_n+\vec{R}(\vec{u}_n)].
\end{aligned}$$

Here $\overleftrightarrow{I}$ denotes the identity matrix.

Since we cannot directly solve the nonlinear algebraic equations (53), we seek their approximate solutions by Picard iteration, known also as a fixed point iteration,

$$\overleftrightarrow{M}(\vec{u}^l)\cdot\vec{u}^{l+1}=\vec{F}(\vec{u}^l)+\vec{G}(\vec{u}^l), \tag{54}$$

where the superscript l denotes the lth iteration. At each time step, the coefficient matrix $\overleftrightarrow{M}$ are evaluated using the solution $\vec{u}^l$ from the previous iteration. The solution at the $(l+1)$th iteration is obtained by solving Eq. (54)

$$\vec{u}^{l+1}=\overleftrightarrow{M}^{-1}(\vec{u}^l)\cdot[\vec{F}(\vec{u}^l)+\vec{G}(\vec{u}^l)]. \tag{55}$$

At the beginning of the iteration, i.e. $l=0$, $\vec{u}^0$ is taken from the converged solution at the previous time, $\vec{u}_n$. The iteration is continued until the difference between $\vec{u}^l$ and $\vec{u}^{l+1}$ reduces to a prescribed convergence criterion. In the present code the convergence criterion is given by

$$\frac{|\vec{u}^{l+1}-\vec{u}^l|}{|\vec{u}^{l+1}|}<\epsilon_{\mathrm{con}}, \tag{56}$$

where $|\ |$ denotes the root-mean-square value of all initially-unknown nodal values and ϵ_{con} is typically chosen as 10^{-5} in the following calculation. Fully converged $\vec{u}^{l+1}$ satisfying the convergence criterion is set as a variable at next time, $\vec{u}_{n+1}$.

While the full-implicit method guarantees numerical robustness, it requires an inversion of the assembled matrix corresponding to $\overleftrightarrow{M}^{-1}$ in Eq. (55). The assembled matrix is constructed by summing up the coefficient matrices derived from element equations to make one global matrix. Since the global matrix is a band matrix, we mainly use the DGBSV routine provided by the LAPACK package [31] with the ATLAS BLAS when inverting coefficient matrix. This routine works faster and has less numerical error than other similar routines.

3.5. SUPG method

In order to eliminate spurious oscillations due to the spatial first derivative, we employ the Streamline Upwind Petrov–Galerkin (SUPG) method. It has been originally developed as a way to suppress spurious oscillations in advection dominated flows in the context of neutral fluid simulations [7], and is basically the upwinding scheme in the finite element method. The advantage of the scheme is that we can obtain a highly accurate solution without increasing the order of the interpolation function. Since we use the piecewise linear interpolation function in our code, the method could work effectively.

Rewriting the radial flow equation Eq. (3) in the s coordinate leads us to

$$\frac{\partial}{\partial t}(rn_su_{sr}) = -2r\frac{\partial}{\partial s}(u_{sr}rn_su_{sr}) + \frac{u_{s\theta}}{r}rn_su_{s\theta} - 2\frac{1}{m_s}s\frac{\partial n_sT_s}{\partial s} + 2\frac{e_s}{m_s}\left(sn_s\frac{\partial \Phi}{\partial s}\right) - \frac{e_s}{m_s}B_\phi rn_su_{s\theta} - 2\frac{e_s}{m_s}s\frac{\partial A_\phi}{\partial s}n_su_{s\phi}. \tag{57}$$

This equation is composed of three terms including the first-order spatial derivative of dependent variables and is similar to advection dominated kind of equation. If one attempt to solve this equation numerically using the usual Galerkin method, one would obtain an oscillating solution, which is unphysical. To avoid this situation, we introduce a modified weight function $\tilde{w}$ for pure advection problems instead of the original one w in the standard Galerkin method as

$$\tilde{w} = w + p\frac{\partial w}{\partial r} = w + 2rp\frac{\partial w}{\partial s}, \tag{58}$$

where p is the factor chosen appropriately. From the Fourier analysis performed by Raymond and Garder [33], the optimal value of p is found to be

$$p \equiv \frac{\Delta r}{15^{1/2}},$$

minimizing the phase error of the solution, where Δr is the element size and is generally dependent on radial position. Through the new weight function including the derivative of the interpolation function, the weak form of Eq. (57) becomes dissipative and the solution will be numerically stable; the derivative term in Eq. (58) acts as the optimal numerical viscosity. The first-order derivative terms appearing in other equations are all convection terms. Their magnitudes are usually much smaller than those of other terms and thus there is no need to use the SUPG method for the equations except the radial flow equation.

4. Simulation results

4.1. Benchmark test

First of all, we have checked the validity of the newly developed code, TASK/TX, by comparing the simulation results with those of the conventional diffusive transport code, TASK/TR [3]. We set initial and boundary conditions as similar as possible to each other, especially profiles of electron density, electron and ion temperatures and safety factor. The TASK/TR code has already been benchmarked [3] with the TOPICS code [34] and with a model profile dataset for benchmark tests provided by International Multi-Tokamak Confinement Profile Database [35].

A set of parameters used in the benchmark test is shown in Table 2. These typical parameters have been partly defined along those of actual medium size tokamaks, JFT-2M where the radial electric field was measured [36]. We assume a plasma composed of electron and hydrogen used in the JFT-2M experiments.

The ways to implement the particle diffusion coefficient and neoclassical transport effects are completely different between the TASK/TX and the TASK/TR codes, so that in this test we assume the turbulent particle transport coefficient and the neoclassical viscous force are set to zero, $D_e = 0, F_{s\theta}^{NC} = 0$. The turbulent perpendicular viscosities μ_s and thermal diffusivities χ_s have been chosen to have parabolic profiles in the radial direc-

Table 2
A set of typical parameters used in the benchmark test

$R = 1.3$ m, $a = 0.35$ m, $b = 0.4$ m, $B_{\phi v} = 1.3$T, $I_p = 0.2$ MA,
$n_{s0} = 0.3 \times 10^{20}$ m^{-3}, $n_{sa} = 0.06 \times 10^{20}$ m^{-3}, $n_{s\mathrm{div}} = 0.01 \times 10^{20}$ m^{-3},
$T_{s0} = 0.5$ keV, $T_{sa} = 0.05$ keV, $T_{s\mathrm{div}} = 0.01$ keV,
$Z_{\mathrm{eff}} = 1.0$, $S_{\mathrm{gas}} = 5.0 \times 10^{18}$m^{-2}s^{-1}, $\gamma = 0.8$

R is the major radius, a the minor radius, b the wall radius, $B_{\phi v}$ the toroidal magnetic field in vacuum, I_p the plasma current, Z_{eff} the effective charge, S_{gas} the neutral influx due to gas puff, γ the recycling rate from the wall and others are defined in Section 2.5.

tion, as already mentioned in Section 2.2.5. The value on the edge is chosen to be 20 times as large as the central one,

$$\chi_s(r) = \begin{cases} \left(1 + 19\frac{r^2}{a^2}\right)\chi_{s0} & (0 \leqslant r \leqslant a), \\ 20\chi_{s0} & (a \leqslant r \leqslant b), \end{cases}$$

and we now choose $\chi_{s0} = 0.25\ \mathrm{m}^2/\mathrm{s}$, resulting in $\chi_s(a) = 5.0\ \mathrm{m}^2/\mathrm{s}$. This profile is also adopted to μ_s.

One of the main differences between the codes is a boundary condition. The TASK/TX code calculates the density and temperature at the plasma surface self-consistently, while the TASK/TR code requires boundary conditions at the surface. Therefore the values at the plasma surface calculated by the TASK/TX code are used in the TASK/TR code as the boundary conditions.

In Fig. 2, we show the results of the benchmark test between these codes at $t = 50$ ms. In spite of the large differences in the basic equations, the results are very similar to each other. We confirmed a good agreement between the electron density profiles in Fig. 2a and the safety factor profile in Fig. 2b in the core region. The difference of the density profile near the plasma edge is due to the ionization which is included only in the TASK/TX code. We note that the slight differences were found in the temperature profiles in Fig. 2c and d: the ion temperature from the TASK/TX code is slightly higher especially near the axis than that from the TASK/TR code. The difference may be attributed to the ohmic heating with a slightly peaked current profile in the TASK/TX code. In conclusion, the TASK/TX code solves the basic terms in the set of equations with sufficient accuracy.

4.2. Typical profiles

Next we show typical ohmic plasma profiles calculated by the TASK/TX code. Basically the plasma parameters used in this and the following sections are the same as those used in the previous section except $Z_{\mathrm{eff}} = 2.0$

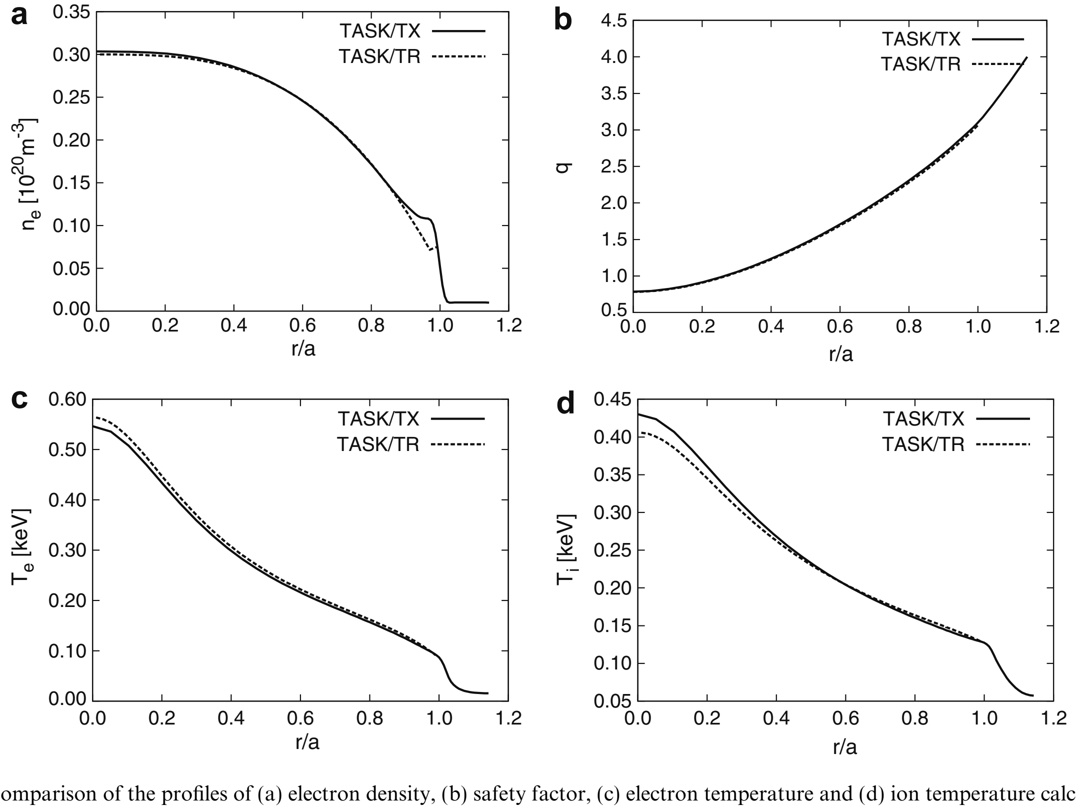

Fig. 2. Comparison of the profiles of (a) electron density, (b) safety factor, (c) electron temperature and (d) ion temperature calculated by the TASK/TX and the TASK/TR code after 50 ms calculation from the initial state.

under the assumption of the existence of a small amount of impurity. Unlike the benchmark test case, the neoclassical effects and the turbulent particle transport are taken into account. Since we are here concerned with a generic behavior of the turbulent diffusion, we assume that turbulent particle transport coefficient D_e has a constant value of $0.03\ \mathrm{m}^2/\mathrm{s}$ over the whole plasma.

In order to clarify a typical behavior of each variable, we show the results of ohmic-heating simulation in Fig. 3, which presents the profiles of sixteen dependent variables described in Table 1, turbulent viscosity, thermal diffusivity, safety factor and toroidal current density at $t = 50$ ms. For these parameters, no edge transport barriers are formed near the plasma surface in the density and temperature profiles, implying that the plasma is in L-mode. The density profile is not in a steady state and the radial velocities are positive over the whole region. The neoclassical inward particle pinch is overwhelmed by the turbulent diffusion of this level. Electron temperature increases due to the ohmic heating power while ion temperature slightly decreases in spite of the energy transfer from electrons. Because of the low poloidal beta of $\beta_p = 0.32$, we can see that the plasma is slightly paramagnetic in the toroidal magnetic field profile: the magnitude at the magnetic axis is 1.5% larger than that at the edge.

4.3. Convergence study

We now examine the numerical convergence under the same plasma condition in the previous section. First, we consider the convergence with respect to the spatial resolution. We varied the number of the spatial mesh

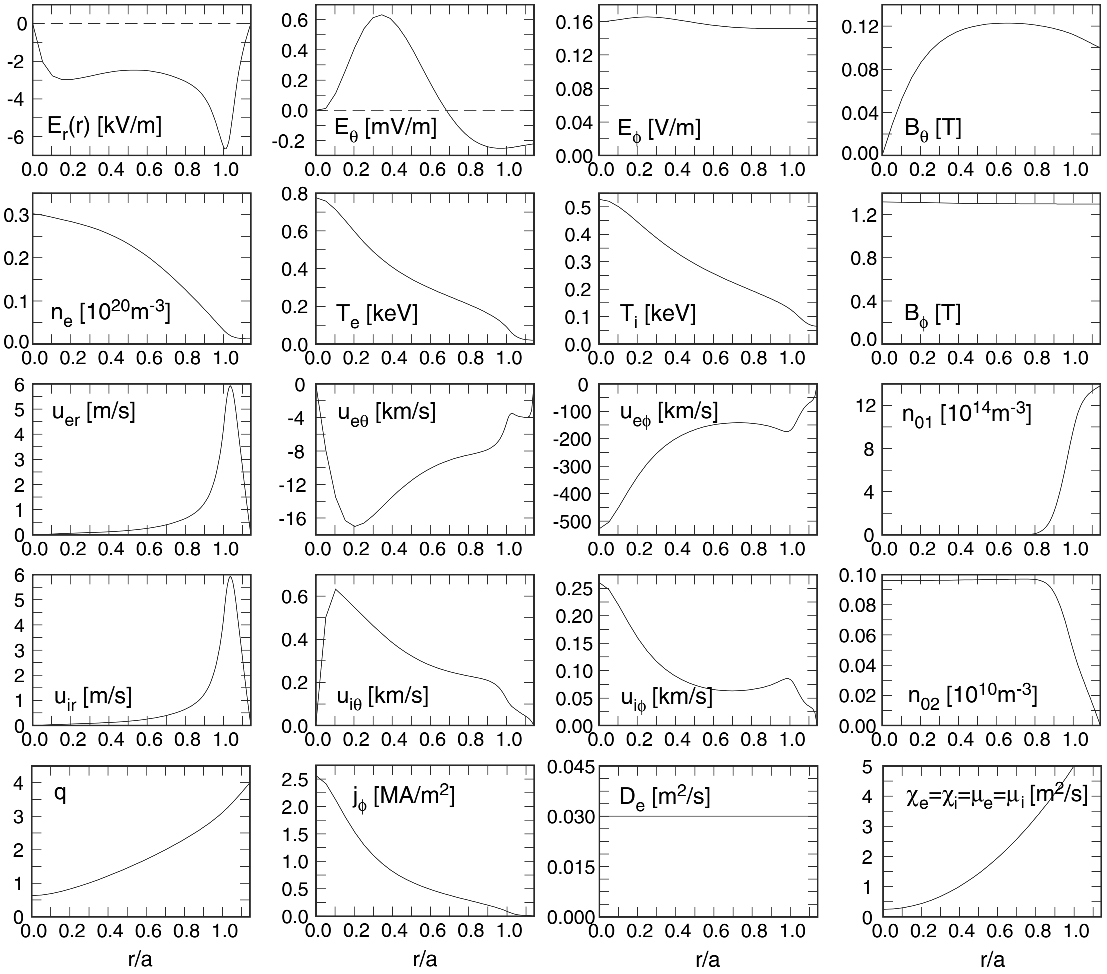

Fig. 3. Typical profiles in an ohmic heated plasma calculated by the TASK/TX code after 50 ms calculation from the initial state.

points from 20 to 100 every 10 interval. The default convergence criterion of Picard iteration in our analyses is 10^{-5} as shown in Eq. (56), which seems to be enough tolerance for nonlinear transport simulations. We then studied how the convergence changes when we vary the convergence criterion, $\epsilon_{\rm con}$ in addition to the change of spatial resolution. We define the arithmetic average number of iterations as the convergence index which is defined by the sum of the number of iterations over all time steps divided by the total number of time steps, 500.

Fig. 4 shows the dependence of the average number of iterations on the number of radial mesh points in four cases: $\epsilon_{\rm con} = 10^{-5}$, 10^{-4}, 10^{-3} and 10^{-2}. When we focus our attention on the average number of iterations for each convergence criterion, we clearly see very weak dependence on the number of spatial mesh points; the average number of iterations gradually grows as the number of mesh points increases. This implies that the solutions of the TASK/TX code converge well almost independent of the number of spatial mesh points for $\epsilon_{\rm con} < 10^{-5}$.

Next we pick up the cases of $N_{\rm max} = 60$ in Fig. 4 and study how the solutions converge when we reduce the convergence criterion from $\epsilon_{\rm con} = 10^{-2}$ to $\epsilon_{\rm con} = 10^{-5}$. By using least-square method, we obtain a fitting function as $N_{\rm ave} = -1.616 \log \epsilon_{\rm con} + 1.557$, where $N_{\rm ave}$ denotes the average number of iterations, which indicates very good exponential convergence.

We should note a larger average number of iterations, $N_{\rm ave}$, in the case of $N_{\rm max} = 100$ and $\epsilon_{\rm con} = 10^{-5}$ in Fig. 4. This increase in iterations is caused by small values of some variable, such as $r\dot{A}_\theta$, in Table 1. According to Eq. (21), $\dot{A}_\theta$ is related to E_θ, which is much smaller than other electromagnetic variables in tokamak plasmas. This type of variables with small values is harder to be converged than other variables and thus generally impedes the rate of convergence when $\epsilon_{\rm con}$ is small.

We also study the dependence of the accuracy of the profile on the convergence criterion. To evaluate the accuracy quantitatively, we introduce a standard deviation σ_n defined by

$$\sigma_n = \sqrt{\frac{\sum_r [f_n(r) - f_{-5}(r)]^2}{\sum_r f_{-5}^2(r)}},$$

where $f_n(r)$ denotes the variable at a radial position r and n is the exponent of $\epsilon_{\rm con}$. We figure out the sum $\sum_r$ over the whole region, $r = 0 \sim b$. By examining this standard deviation, we are able to evaluate the difference between the profile for given $\epsilon_{\rm con}$ and the corresponding profile at $\epsilon_{\rm con} = 10^{-5}$. We now choose $N_{\rm max} = 60$ and calculate the standard deviations at $t = 50$ ms.

From Table 3, we confirm that profiles for any variables steadily converge with the profiles at $\epsilon_{\rm con} = 10^{-5}$ when we gradually reduce the convergence criterion from 10^{-2} to 10^{-5}. We should note that the profiles at $\epsilon_{\rm con} = 10^{-2}$ are sufficiently accurate with the standard deviations less than 10^{-6} for most variables.

We now focus our attention to $r\dot{A}_\theta$ in Table 3. Its standard deviations are more than one order larger than any other deviations for all $\epsilon_{\rm con}$'s and we see that $r\dot{A}_\theta$ is a bottleneck in convergence. We also found from Table 3 that the more important potentials such as ϕ, $\dot{A}_\phi$ and rA_θ are sufficiently accurate even if we adopt loose criterion.

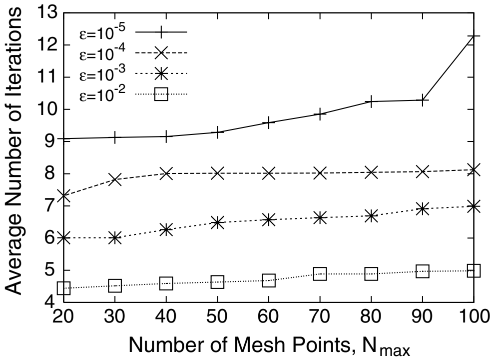

Fig. 4. Dependence of arithmetic average of the number of iterations on the number of spatial mesh points in four cases from $\epsilon_{\rm con} = 10^{-5}$–$10^{-2}$.

Table 3
Standard deviations of all the variables except for beam ion components

ϵ_{err}	10^{-4}	10^{-3}	10^{-2}
ϕ	6.89 (−9)	5.77 (−8)	6.49 (−7)
$r\dot{A}_\theta$	2.15 (−7)	9.81 (−7)	1.46 (−5)
$\dot{A}_\phi$	4.55 (−9)	5.99 (−8)	4.10 (−7)
A_ϕ	9.84 (−10)	1.62 (−8)	7.92 (−7)
rA_ϕ	1.90 (−12)	3.25 (−11)	6.02 (−10)
n_e	4.12 (−9)	2.85 (−8)	2.44 (−7)
$rn_\mathrm{e}u_{\mathrm{e}r}$	2.08 (−8)	1.06 (−7)	5.06 (−7)
$rn_\mathrm{e}u_{\mathrm{e}\theta}$	1.07 (−8)	3.18 (−8)	7.24 (−7)
$n_\mathrm{e}u_{\mathrm{e}\phi}$	3.25 (−9)	1.98 (−8)	9.44 (−7)
$n_\mathrm{e}T_\mathrm{e}$	3.03 (−9)	2.04 (−8)	2.61 (−7)
n_i	4.12 (−9)	2.85 (−8)	2.44 (−7)
$rn_\mathrm{i}u_{\mathrm{i}r}$	2.08 (−8)	1.06 (−7)	5.06 (−7)
$rn_\mathrm{i}u_{\mathrm{i}\theta}$	7.55 (−8)	4.51 (−7)	7.89 (−7)
$n_\mathrm{i}u_{\mathrm{i}\phi}$	3.23 (−9)	2.90 (−8)	9.84 (−7)
$n_\mathrm{i}T_\mathrm{i}$	3.14 (−9)	3.57 (−8)	5.39 (−7)
n_{01}	8.37 (−9)	5.10 (−8)	8.93 (−8)
n_{02}	1.33 (−8)	1.22 (−7)	6.51 (−7)

Numbers in the parentheses denote the power of ten; for example, 6.89(−9) means 6.89×10^{-9}.

Finally it is worth noting how the number of iterations depends on the time step as well as the iteration tolerance. Due to the electron parallel heat loss model in the SOL, $\nu_{\mathrm{L}T_\mathrm{e}}$, which is a strongly nonlinear function of the electron temperature, the upper limit of the time step is inevitably imposed: $\Delta t \approx 2.5 \times 10^{-4}$ s. If we use a larger time step above this criterion, the profile of the electron temperature in the SOL would alternate between the higher and the lower temperature states every time step. We then focus on the convergence dependence in the range of $10^{-6} \leqslant \Delta t \leqslant 2.5 \times 10^{-4}$. $N_{\max} = 60$ is chosen and we calculate the average number of iterations after 10 ms calculation: 10^4 time steps are needed in the case of $\Delta t = 10^{-6}$ and 40 time steps in the case of $\Delta t = 2.5 \times 10^{-4}$. From Fig. 5a, we find the tendency that regardless of the convergence criterion the average number of iterations decreases as the time step size decreases. However we also find increases in the number of iterations in the smaller time step size region.

From the analysis using the standard deviation shown in Table 3, we have already known that the convergence speed of $r\dot{A}_\theta$ is slower than other variables. The ion toroidal velocity in the ohmic heating phase is very small compared with other flows. Furthermore, the convergence speed of $r\dot{A}_\phi$ tends to be slower due to the displacement current term. We therefore carry out the convergence test with relaxed convergence criteria for $r\dot{A}_\theta$ and $n_\mathrm{i}u_{\mathrm{i}\phi}$ by 10^2 and that for $r\dot{A}_\phi$ by 10. As shown in Fig. 5b we can see mostly monotonic dependence

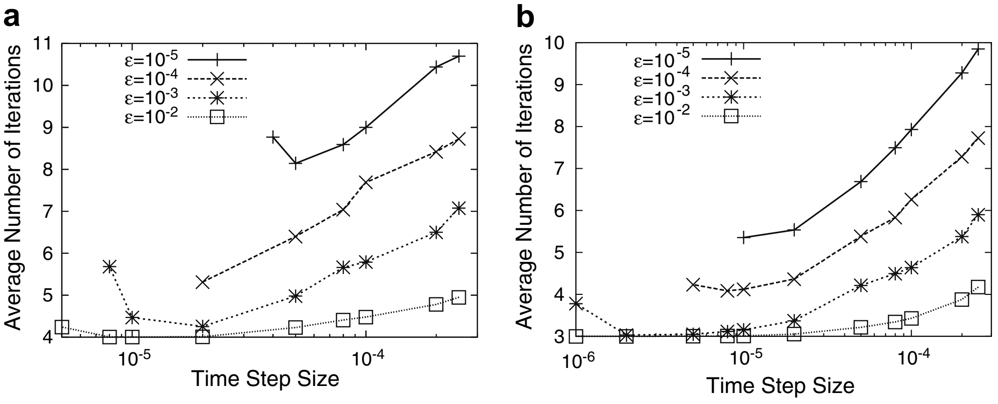

Fig. 5. Dependence of arithmetic average of the number of iterations on the time step size in four cases from $\epsilon_{\mathrm{con}} = 10^{-5}$ to 10^{-2}. In the case (a), the same convergence criterion is imposed on all the equations while, in the case (b), the loose convergence criterion is adopted only in the equations of $r\dot{A}_\theta$, $r\dot{A}_\phi$ and $n_\mathrm{i}u_{\mathrm{i}\phi}$.

of the average number of iterations on the time step size: We should note that the solutions are not converged when the time step size is smaller than $\Delta t = 10^{-5}$ for $\epsilon_{\mathrm{con}} = 10^{-5}$ and 10^{-4}. The failure of convergence for $\Delta t \lesssim 10^{-5}$ may be attributed to the existence of compressional Alfvén wave with frequency range of ~ 100 kHz.

4.4. Neoclassical transport without turbulence

In order to clarify how the neoclassical transport works in the simulations by the TASK/TX code, it is useful to consider a stationary profile without turbulent transport. In other words, $D_{e0} = \chi_{s0} = \mu_{s0} = 0$. Since the TASK/TX code includes only the neoclassical particle flux, we now concentrate on a particle transport phenomenon, keeping the temperature profiles fixed to the initial ones in this section. The set of plasma parameters and initial profiles is basically the same as that in the previous section except the plasma current and the rate of gas puff: the former is reduced to $I_{\mathrm{p}} = 0.12$ MA and the latter is also reduced to $S_{\mathrm{gas}} = 1.0 \times 10^{18}\ \mathrm{m}^{-2}\ \mathrm{s}^{-1}$ for the purpose of accelerating the relaxation towards a steady state. The calculation is stopped at $t = 500$ ms where the plasma reaches a quasi-steady state.

In Fig. 6a, a peaked density profile is observed. This is caused by the Ware pinch due to the neoclassical effect, which is described in the second term of Eq. (38). As can be seen in Fig. 6b, the inward radial flux is very small but still exists in the core region. The inward flux in the outer region, $0.8 \lesssim r/a \lesssim 0.95$, balances with the ionization of neutrals in Fig. 6d. The outward flux in the edge region, $0.95 \lesssim r/a \lesssim 1.05$, is due to the ionization inside the plasma surface and the parallel loss outside it.

The radial electric field shows a large negative peak at the plasma edge region ($r \approx a$) in Fig. 6b. This peak partly stems from the difference between the neoclassical diffusivities of electrons and ions. Since the transport in the SOL is dominated by the parallel transport, there exists an abrupt change of transport mechanism at the plasma edge. The ions which have larger radial diffusivity due to the larger orbit size escape to the SOL slightly quicker than the electrons. More electrons are therefore left on the inner side of the plasma edge, while ions accumulate on the outer side, i.e. the SOL, where both electrons and ions are lost to the divertor with the same

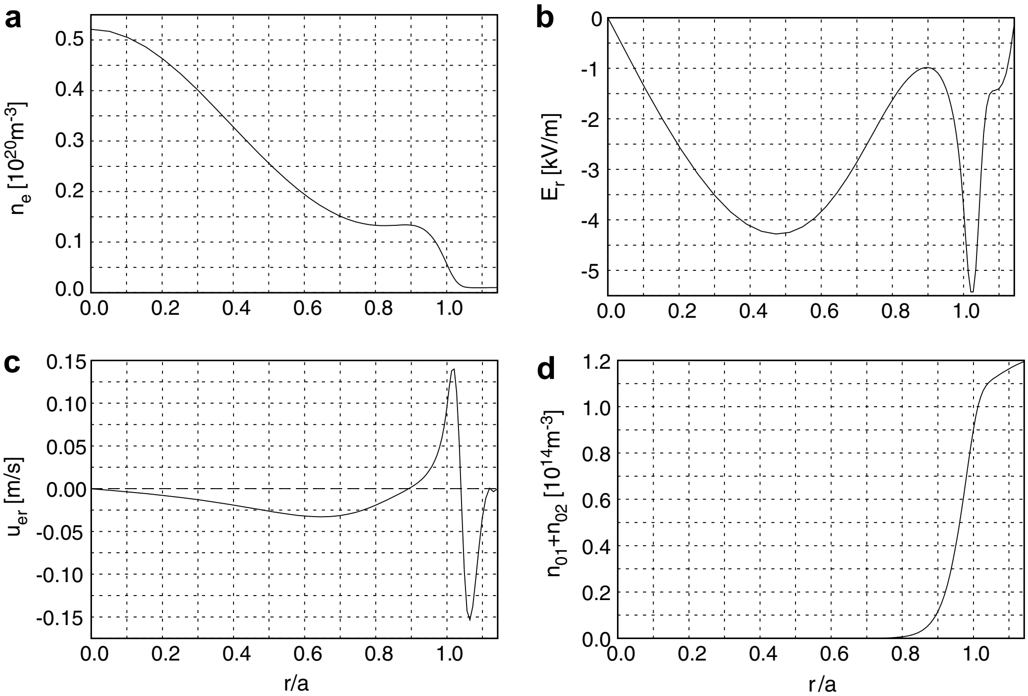

Fig. 6. The radial profiles of the (a) electron density, (b) radial electric field, (c) electron radial velocity and (d) neutral density without turbulent transport at $t = 500$ ms.

loss rate. The localized electric field also drives a poloidal rotation of electrons and ions and it affects the radial flux and then the density profile.

4.5. Turbulent transport without neoclassical effect

In our model equations, we do not use the particle diffusion equations for electrons and ions; the density is described by the continuity equation, Eq. (2) and we do not assume the particle diffusion explicitly in the equation. If turbulent fluctuations exist, a force induced by them damps the poloidal velocity and then affects the radial velocity through the poloidal force balance in Eq. (4), and finally particles may diffuse owing to the advective term. We should therefore confirm whether the particles actually diffuse by this mechanism. For this purpose, we carried out a simulation without the neoclassical viscosity $\nu_{\mathrm{NC}s}$. The parameters and conditions are the same as those in Section 4.2.

The simulation results of the electron density profile are shown in Fig. 7. Diffusion observed in Fig. 7a clearly confirms that the model poloidal force induces particle diffusion. In addition, we carry out the simulation without not only the neoclassical viscosity but also the turbulent particle diffusivity D_{e}. In this case, as expected, the density profile hardly changes in the core plasma and no diffusion and pinch are observed in Fig. 7b. In the vicinity of the plasma surface, ionization due to the neutral influx inside the plasma surface and the parallel loss in the SOL modify the shape of the density profile.

4.6. Validity of the neoclassical model

As described in Section 2.2.4, we introduced only the neoclassical poloidal viscosity to describe all the neoclassical effects in the TASK/TX code. We cannot therefore distinguish an individual neoclassical effect from a simulation result; e.g. the toroidal current includes the bootstrap current, but we cannot directly calculate the fraction of the bootstrap current in the total current.

When the plasma approaches to a steady state, we may use the analytic solutions Eqs. (38) and (39) in a steady state given in Section 2.3 to estimate the value of the resistivity and bootstrap current. The resistivity given in Eq. (40) and the bootstrap current obtained from the second term in the angled bracket in Eq. (39) are written as:

$$\eta_{\parallel} = \frac{m_{\mathrm{e}}(1+\alpha)\bar{\nu}_3}{n_{\mathrm{e}}e^2}\frac{B_\phi^2}{B^2}, \tag{59}$$

$$j_{\mathrm{BS}_\parallel} = -\frac{1}{1+\alpha}\frac{B_\theta}{BB_\phi}\frac{\nu_{\mathrm{NCe}}}{\bar{\nu}_3}\frac{\partial p}{\partial r}. \tag{60}$$

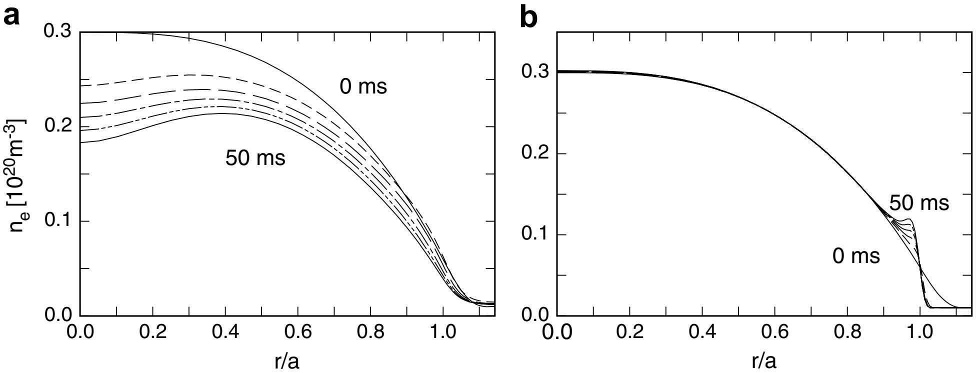

Fig. 7. The electron density profiles. The figure (a) shows the result without neoclassical viscosity $\nu_{\mathrm{NC}s}$ and the figure (b) shows the result with neither neoclassical viscosity nor turbulent particle diffusivity D_{e}. 0 ms denotes the initial profile and 50 ms the final profile of the simulation. Each line is drawn at every 10 ms in both figures.

To assess the validity of our neoclassical model, we now compare the neoclassical resistivity and bootstrap current calculated by Eqs. (59) and (60) with those calculated directly in the NCLASS module and the approximate formula of Sauter model [37]. In this subsection, we ignore the potato orbit effect because the Sauter model does not take account of it.

Before the comparison, we also note that only in this subsection we assume flat temperature profiles in the core plasma in order to exclude the effect of a neoclassical heat flux driven by the temperature gradient. Given the same set of parameters in Section 4.2 except the effective charge of $Z_{\mathrm{eff}} = 1.0$ and the flat temperature profiles, the resistivity and bootstrap current has been calculated using the initial profiles. The result of comparison is presented in Fig. 8. The Sauter model provides almost the same profiles as the NCLASS results. For both the resistivity and the bootstrap current, the profiles of the steady-state estimates in the TASK/TX code and the NCLASS results are similar in shape and the magnitude of them are comparable with each other. For both resistivity and bootstrap current, the discrepancies between the TASK/TX and the NCLASS results are less than 20%.

4.7. Parameter dependence

It is important to clarify the dominant parameter dependence of plasma behavior in the TASK/TX code. In this section, we change several plasma parameters around the reference values used in Section 4.2 in order to study a response of the plasma. All the results in this section are collected at $t = 50$ ms same as the case of the typical profile in Section 4.2.

4.7.1. Turbulent particle diffusivity

The turbulent particle diffusivity strongly affects the particle transport and thus the momentum transport. With the change of D_{e} in the turbulent induced force terms, $F_{s\theta}^{\mathrm{W}}$ and $F_{s\phi}^{\mathrm{W}}$, the density profile indirectly changes through the change of the radial flux as we have seen in Section 4.5. The case of low diffusivity ($D_{\mathrm{e}} = 0.01\ \mathrm{m}^2/\mathrm{s}$) is similar to that of no turbulent diffusivity case, viz. only the neoclassical effect. The particles hardly diffuse because of the low diffusivity and due to the neoclassical viscosity the inward pinch dominates the density profile in the core. It then peaks on the magnetic axis as shown in Fig. 9. The radial electric field peaks at the plasma surface because the lower diffusivity allows the pressure profile to be steep. The electron temperature becomes comparable to the ion temperature owing to the high density.

The inward pinch gradually decreases with the increase in D_{e} because the diffusion process overcomes the pinch. In the case of $D_{\mathrm{e}} = 0.03\ \mathrm{m}^2/\mathrm{s}$, the inward pinch almost vanishes and the positive radial flux prevails over the whole plasma, resulting in the flat profile of the density near the axis. With the further increase in D_{e}, the density near the axis drops in a transient phase.

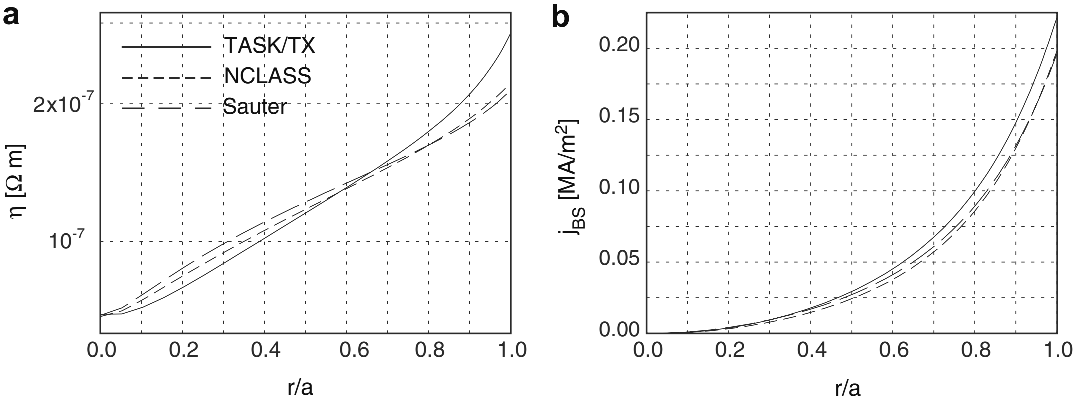

Fig. 8. Comparison of (a) the neoclassical resistivity and (b) the bootstrap current between analytic solutions given in Eqs. (59) and (60) (solid line) and the results from the NCLASS module (broken line) and the Sauter model (long broken line) with flat temperature profiles in the initial state.

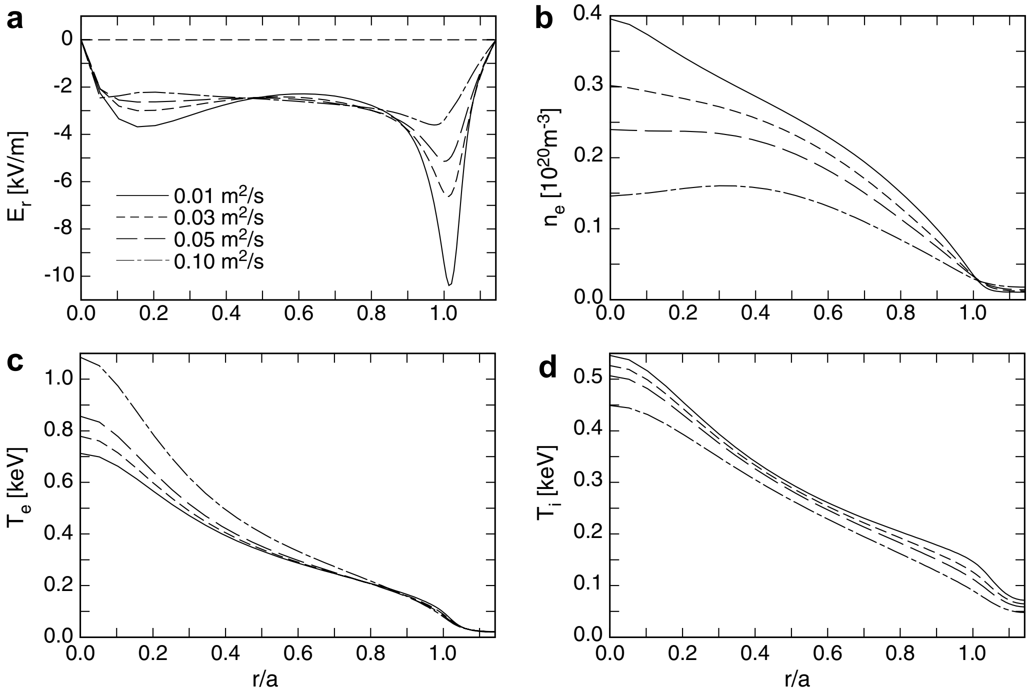

Fig. 9. Parameter dependence of the radial profiles on the turbulent particle diffusivity D_e: (a) the radial electric field E_r, (b) the electron density n_e and (c) the electron and (d) the ion temperatures, T_e and T_i, respectively.

4.7.2. Plasma current

The total plasma current affects not only the poloidal magnetic field, but also all the plasma variables through the Ware pinch and Joule heating.

In Fig. 10, we show the cases of $I_p = 0.15$ MA, 0.2 MA and 0.25 MA. Increase in I_p directly ramps up j_ϕ and then E_ϕ, leading to enhancement of ohmic heating power. Ohmic heating power increases T_e and then T_i through the energy exchange. Increase in the ion temperature causes the ion pressure to increase, then leading to increase in the magnitude of E_r because the radial electric field is mostly governed by the ion pressure gradient unless strong rotations exist. Increase in E_ϕ also induces enhancement of the Ware pinch. This inward pinch makes more particles move inward and then the density slightly peaks near the axis.

4.7.3. Gas puff and recycling rate

Neutral influxes by a gas puff and recycling directly affect the thermal neutral density and they may affect the density profile of the core plasma. With the increase of the neutral density in the SOL, the plasma density may increase due to the ionization. In order to study the influence of the neutral influx from the wall, we vary the influx by the gas puff $S_{\text{gas}} = 1.0 \times 10^{18}$, 5.0×10^{18} and 1.0×10^{19} m^{-2} s^{-1} and the recycling rate $\gamma = 0.5$, 0.8 and 0.9.

The change of these factors leads to little change of density profile. The densities of the thermal and fast neutrals increase in proportion to the neutral influx. Owing to the increase of neutral densities, the ionization process makes more charged particles in the SOL and then the plasma density rises. According to the increase of the plasma density, the magnitude of the radial electric field in the region of $r/a > 0.6$ slightly decreases. The change of the neutral densities in the SOL, however, hardly affects the variables in the core region and the effect on those in the SOL is limited although it depends on the velocity of the neutrals bounced back from the wall. The change of the neutral influx from the wall does not affect the core plasma so much for the present plasma parameters.

4.7.4. NB injection

Next we describe the behavior of the plasma under the NBI heating with co and counter injections relative to the plasma current.

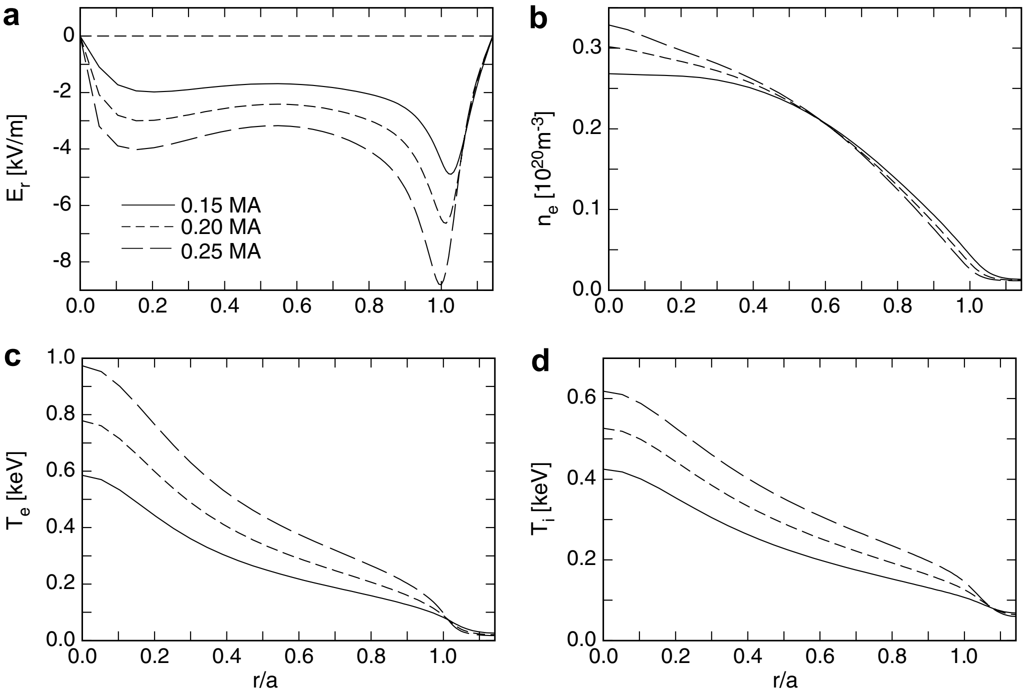

Fig. 10. Parameter dependence of the radial profiles on the plasma current I_p: (a) the radial electric field E_r, (b) the electron density n_e and (c) the electron and (d) the ion temperatures, T_e, T_i, respectively.

In the simulation with NBI, we assume the following shape of beam deposition profile:

$$P_b(r) = P_{b0} \exp\left(-\frac{r^2}{r_{NB}^2}\right)[1-(r/a)^4]$$

where P_{b0} is the normalization factor determined by the way that the integral of $P_b(r)$ in a plasma is equal to the total heating power. On-axis power deposition profile is assumed. r_{NB} denotes the heating width of NBI and typically $r_{NB} = 0.15$ m. The beam energy $E_b = 32$ keV and the heating power 0.5 MW are chosen according to the NBI experiment on JFT-2M [36]. We have assumed $D_e = 0.01\ \mathrm{m}^2/\mathrm{s}$, $\chi_s(0) = 0.5\ \mathrm{m}^2/\mathrm{s}$ and $\mu_s(0) = 1\ \mathrm{m}^2/\mathrm{s}$. The dependence on D_e will be discussed later. The values of μ_s and χ_s were adjusted to roughly reproduce the experimental peak values of toroidal rotation velocity and temperatures on JFT-2M. We now study three cases in this subsection: (i) ohmic heating case at $t = 20$ ms just before the NBI starts, (ii) co NBI case at $t = 100$ ms, (iii) counter NBI case at $t = 100$ ms. The results are presented in Fig. 11.

The input of the toroidal momentum from NBI strongly rotates the beam ions in the toroidal direction (Fig. 11l). The bulk ions rotate toroidally in the same direction due to the collisional momentum transfer from the beam ions (Fig. 11i). The electrons follow the bulk ions with a slightly slower toroidal velocity due to the collisional drag with $Z_{\mathrm{eff}} > 1$ (Fig. 11f). Before the NBI starts, the radial electric field E_r is mostly determined by the ion pressure gradient. After the NBI starts, however, the fast ion toroidal velocity dominantly governs the behavior of E_r through Eq. (3). We observe positive E_r in the co-injection case and strongly negative E_r in the counter-injection case (Fig. 11d).

We observe density profile modification due to the NBI (Fig. 11a). There are two mechanisms inducing radial particle flux. One is the neoclassical flux driven by the beam ions, the fourth term in Eq. (38). This flux is outward for co-injection and inward for counter-injection. The other is the turbulence-induced flux, the third term in Eq. (38), which is mainly driven by the friction force, Eq. (36). Since the beam ions drag the electrons and the electrons tend to move along the field line ($u_{e\theta} > 0$ for $u_{i\phi} > 0$), $F_{e\theta}^{W}$ is negative in the co-injection case and positive in the counter-injection case. Therefore the turbulence-induced flux is inward for co-injection and outward for counter-injection.

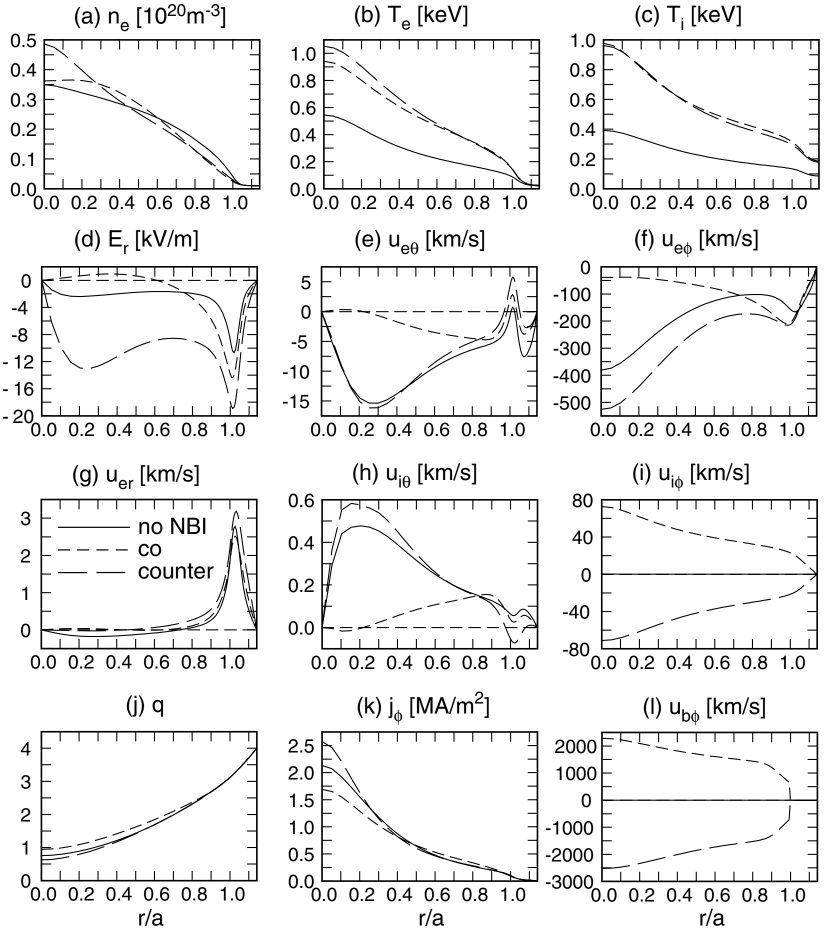

Fig. 11. Parameter dependence of the NBI heating power and its direction: (a) the electron density n_e, (b) the electron and (c) the ion temperatures, T_e, T_i, (d) the radial electric field E_r, (e) the electron poloidal and (f) toroidal velocities, $u_{e\theta}, u_{e\phi}$, (g) the electron radial velocity u_{er}, (h) the ion poloidal and (i) toroidal velocities, $u_{i\theta}, u_{i\phi}$, (j) the safety factor q, (k) the toroidal current j_ϕ and (l) the beam ion toroidal velocity $u_{b\phi}$.

Since the neoclassical and the turbulence-induced fluxes are in opposite directions, the total particle flux depends on the magnitude of D_e; in the case of co-injection, the flux is outward for small D_e and inward for large D_e. For the present value of $D_e = 0.01$ m^2/s, the neoclassical flux is still dominant. In the case of co-injection, therefore, the outward flow allows the density profile to flatten near the magnetic axis, while the density profile is peaked in the case of counter-injection (Fig. 11a).

Next we look at the change of the electron temperature. In the case of co-injection, the direction of the beam driven current is the same as that of the plasma current. Since the total current is fixed in the present calculations, the ohmic current is largely replaced by the beam-driven current and the Joule heating decreases. In the case of counter-injection, the counter current drive increases the ohmic current and enhances the Joule heating, leading to higher T_e compared with the case of co-injection. In this JFT-2M like plasma, the initial beam energy E_b is much greater than the critical energy E_c over the whole plasma except near the magnetic axis, hence the beam mainly heats the electrons rather than the ions. Thus the electron temperature increases shortly after the start of the NBI. The electron temperature, however, equilibrates to the ion temperature owing to the energy equipartition as the plasma approaches to a steady state. In the co injection case, since the ions are heated due to the momentum deposition heating in addition to the collisional heating, the ion temperature is larger than the electron one unlike the counter injection case.

Finally, we study how well the present TASK/TX code is able to reproduce the experimental profile observed on JFT-2M. Although given parameters and initial conditions are almost the same as the previous simulation, in this case we have assumed $D_e = 0.025\ \mathrm{m}^2/\mathrm{s}$, $\mu_s(0) = 1.3\ \mathrm{m}^2/\mathrm{s}$, $\chi_i(0) = 2\chi_e(0) = 0.9\ \mathrm{m}^2/\mathrm{s}$ and $S_{\mathrm{gas}} = 3.0 \times 10^{20}\ \mathrm{m}^{-2}\mathrm{s}^{-1}$. The initial electron density and temperatures on the magnetic axis, $n_e(0) = 0.24 \times 10^{20}\ \mathrm{m}^{-3}$, $T_e(0) = 0.7\ \mathrm{keV}$ and $T_i(0) = 0.4\ \mathrm{keV}$, are taken from Fig. 1c at $t = 550\ \mathrm{ms}$ in Ref. [36], when the co NBI was activated. We concentrate on the case with co NBI phase corresponding to $t = 550$–$750\ \mathrm{ms}$ in the experiment. According to the experiment, the code runs with the co NBI of $P_{\mathrm{NB}} = 0.5\ \mathrm{MW}$ for 200 ms. We compared the profiles of the radial electric field and the ion toroidal velocity with those observed in the experiment in Fig. 12a and b at $t = 690\ \mathrm{ms}$ in the experiment corresponding to $t = 140\ \mathrm{ms}$ in the simulation. Although the results do not perfectly agree with the experiment, the magnitude and the shape of the profiles in the core region are similar, although the behavior of $u_{i\phi}$ in $r/a > 0.6$ is different. Time evolutions of the electron and ion temperatures on the magnetic axis and the ion toroidal velocity at $r/a = 0.15$ are compared with the experiment in Fig. 12c and d. The temperatures in the simulation grow more rapidly than those of the experiment, but $T_{e,\mathrm{sim}}(0)$ finally reaches the experimentally observed electron temperature. This rapid increase in the initial phase can also be seen in the $u_{i\phi}(r/a = 0.15)$ evolution.

4.7.5. Ion orbit loss effect

The TASK/TX code does not assume the quasi-neutrality, which distinguishes itself from other conventional transport codes. We will, therefore, show one example of the capability of the TASK/TX code which can deal with a problem of breaking the quasi-neutrality.

In the edge region, ion orbits with large radial excursions are apt to intersect the wall boundary and are lost from the confinement region. Sudden lack of ions may produce the inward radial electric field, which pulls ions back in the confinement region and pushes electrons outside the plasma. It is believed that a sudden increase of the ion orbit loss is a candidate for the trigger for the L–H transition [38]. Therefore, it is important to know how the radial electric field develops with the ion orbit loss and how it affects the plasma state.

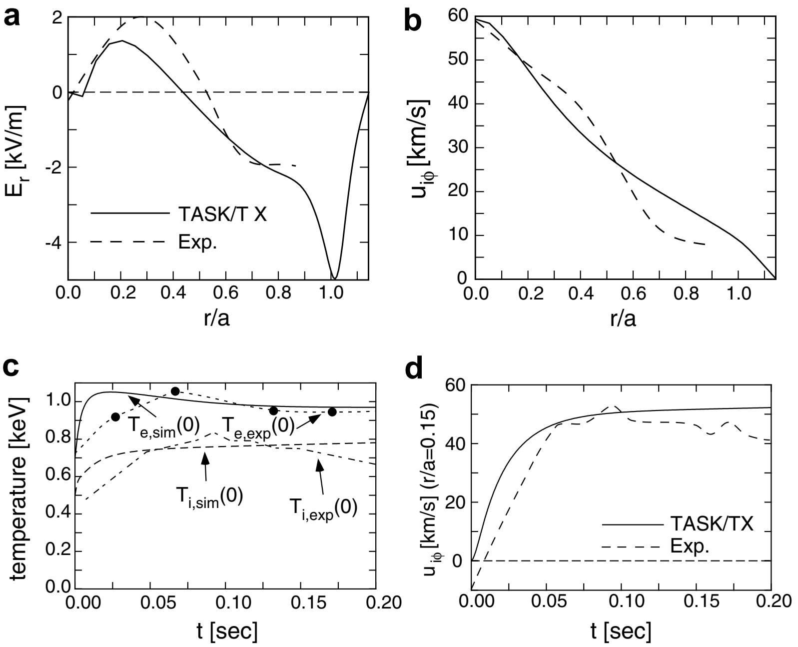

Fig. 12. Comparison of the radial profiles of (a) the radial electric field and (b) the ion toroidal velocity at $t = 140\ \mathrm{ms}$, and the time evolutions of (c) the temperatures on the magnetic axis and (d) the ion toroidal velocity at $r/a = 0.15$ between the simulation result and the experiment on JFT-2M [36]. The experimental profiles are taken from Fig. 1a, c and Fig. 2a and b in Ref. [36]. Filled circles and the broken line (expressed as $T_{e,\mathrm{exp}}(0)$) found in (c) denote the measured values from observation and their interpolation line, respectively.

Conventional transport codes generally solve one continuity equation for either electrons or ions since they explicitly assume the quasi-neutrality condition. These codes cannot self-consistently deal with the problem that the ion particle flux $\Gamma_{\rm i}$ exceeds the electron one $\Gamma_{\rm e}$. In the TASK/TX code, however, simple addition of the ion orbit loss term to the continuity equation and corresponding momentum equations causes various effects induced by the ion orbit loss self-consistently.

For ions, we introduce the ion orbit loss terms

$$S_{\rm i}^{\rm iL} = -\nu_{\rm iL} n_{\rm i}$$

$$F_{\rm i\theta}^{\rm iL} = -\nu_{\rm iL} n_{\rm i} u_{\rm i\theta}$$

$$F_{\rm i\phi}^{\rm iL} = -\nu_{\rm iL} n_{\rm i} u_{\rm i\phi}$$

to Eqs. (2), (4) and (5), respectively. Here $\nu_{\rm iL}$ is the ion orbit loss rate defined by [39]

$$\nu_{\rm iL} = \frac{2.25}{\pi^{1/2}} \frac{\nu_t}{(2|S|\epsilon)^{1/2}} \exp\left[-\left(\nu_*^{1/4} + \frac{\Omega_{\rm i}|S|^{1/2}}{I v_{\rm thi}} \frac{|\psi - \psi_s|}{(2\epsilon)^{1/2}}\right)^2\right],$$

where ν_t is the deflection collision frequency evaluated at $v = v_{\rm thi}$, ϵ is the inverse aspect ratio, $\nu_* = \nu_t Rq/[v_{\rm thi}(|S|\epsilon)^{3/2}]$, $\Omega_{\rm i} = Z_{\rm i}eB/m_{\rm i}$, $I = RB_\phi$, and ψ is the poloidal flux and the subscript s denotes the plasma surface. Here S is the orbit squeezing factor given by $S = 1 - (\rho_{pi} d\ln E_r/dr)(E_r/B_\theta v_{\rm thi})$ [40], where ρ_{pi} denotes the ion poloidal gyroradius. In this model the ion orbit loss rate depends on the shear of the radial electric field through the orbit squeezing term.

For this ion orbit loss simulation, we have modified the boundary conditions. In a transient phase, it is anticipated that the radial current flows due to $\Gamma_{\rm i} > \Gamma_{\rm e}$, so that the boundary condition of $u_{sr} = 0$ at $r = b$ is no longer appropriate. Therefore we set the density gradient to zero at the boundary instead of $u_{sr} = 0$.

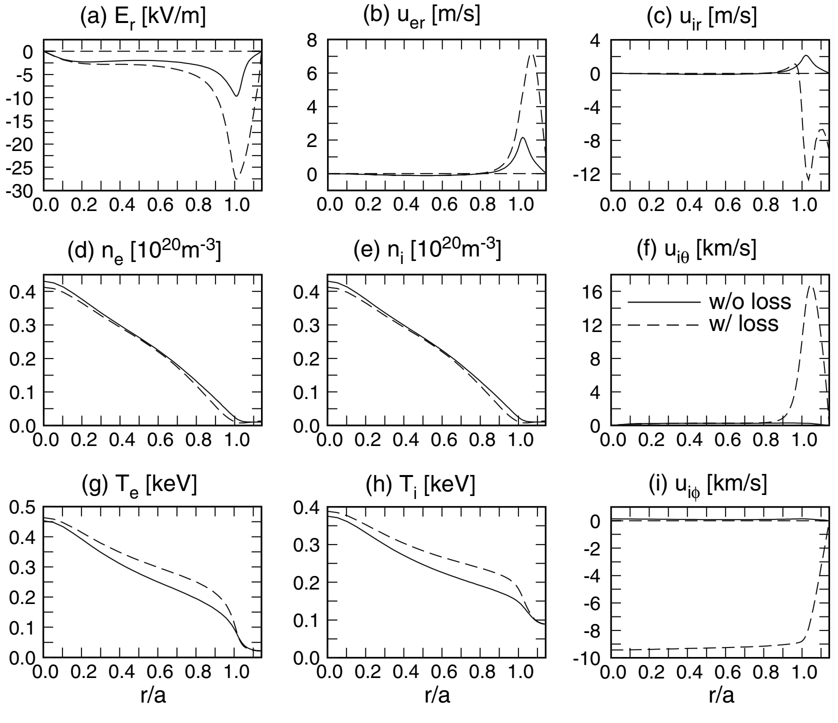

Fig. 13. Comparison of the radial profiles between the cases with and without the ion orbit loss in an ohmic heating plasma at $t = 100$ms: (a) the radial electric field E_r, (b) the electron and (c) ion radial velocities, $u_{\rm er}$, u_{ir}, (d) the electron and (e) ion densities, $n_{\rm e}$, $n_{\rm i}$, (f) the ion poloidal velocity $u_{\rm i\theta}$, (g) the electron and (h) ion temperatures, $T_{\rm e}$, $T_{\rm i}$, and (i) the ion toroidal velocity $u_{\rm i\phi}$.

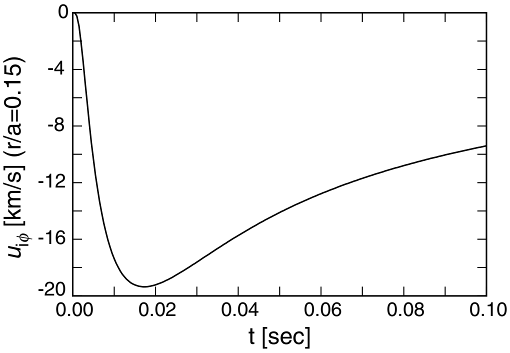

Fig. 14. Time evolution of the ion toroidal velocity $u_{i\phi}$ at $r/a = 0.15$.

Under the same condition as the ohmic phase of the NB injection case in previous section, the simulation was carried out for 100 ms. We then compare the cases with and without the ion orbit loss in Fig. 13. A sudden loss of ions around the plasma surface breaks the quasi-neutrality and in order to compensate the difference of the density the strong inward radial electric field is produced there (Fig. 13a), leading to the outward electron flux and inward ion flux (Fig. 13b and c). The ion density drops near the plasma surface due to the loss channel of the ions and the electron density follows it (Fig. 13d and e). With the change of the densities, the pedestal of the temperatures for both electrons and ions develops (Fig. 13g and h). This implies that the pedestal of the pressure hardly changes. The poloidal velocity is damped by the neoclassical viscosity in the core confinement region, but it greatly rotates near the plasma surface owing to the torque induced by the ion orbit loss (Fig. 13f). The situation is the same for the ion toroidal velocity (Fig. 13i). The ion orbit loss induces the inward radial current in the proximity of the peripheral, which produces the torque in the presence of the magnetic field. The torque makes the plasma rotate near the plasma surface, and then the perpendicular viscosity diffuses the produced momentum towards both sides. There is no significant damping mechanism in the toroidal direction in comparison with the poloidal direction, hence after a short time, the toroidal rotation profile becomes uniform in the core region.

Since there is no net current across the flux surface in a steady state, no net torque is applied on the plasma [39]. In other words, the rotation is gradually been damped in a transient phase, and finally the rotation will stop. The time evolution of the ion toroidal velocity at $r/a = 0.15$ shown in Fig. 14 confirms the damping of the rotation in the simulation. We found that the relaxation time of the toroidal velocity is relatively long and finite. The toroidal velocity remains even if we proceed the simulation further. This implies that the ion orbit loss may be a candidate for the origin of the spontaneous (intrinsic) rotation.

5. Conclusion and discussion

A new one-dimensional transport code, TASK/TX, has been developed to describe time evolution of a plasma in a circular cylindrical geometry. We have assumed that the transport along the magnetic field line is much faster than the phenomena of our interest in order to employ the magnetic surface average. This code calculates not only the particle density and temperature but also the radial particle flux and poloidal and toroidal rotations self-consistently, by solving a set of flux-surface averaged two-fluid equations coupled with Maxwell's equations, neutral diffusion equations and beam slowing-down equations. These dynamic transport equations also describe the time evolution of the radial electric field, which is believed to play an important role for improved confinement. Unlike the conventional one-dimensional transport code based on the flux-gradient relation, the code also describes the transient phenomena on a rapid time scale because equations of motion are solved. These equations are calculated over the whole plasma including the SOL, so that it is not necessary to impose explicit boundary conditions on the plasma surface; alternatively the values at the plasma surface are determined by the balance between the core and SOL transport. In this model, explicit particle diffusivity does not appear in the continuity equations (particle transport equation). The particle diffusion is expressed in the convective flux due to the perpendicular friction force in the poloidal and toroidal equations. It was confirmed through the steady state analysis that the model equations including the neoclassical viscosity express the important neoclassical effects, such as the Ware pinch, the resistivity and the bootstrap current.

In order to solve the set of the dynamic transport equations, the finite element method is adopted because mesh accumulation near the plasma surface is crucial to describe the abrupt change of plasma quantities due to the difference of transport mechanisms. For robust calculation, several numerical stabilization schemes have been introduced. First, by transforming the spatial coordinate of the equations from r to $s(=r^2)$, the natural boundary conditions at the magnetic axis of $\partial/\partial r|_{r=0}=0$ are automatically satisfied. Secondly, the dependent variables are carefully chosen to be suitable for the linear interpolation function. Finally the Streamline Upwind Petrov–Galerkin (SUPG) method has been introduced in the radial component of the equations of motion including the advective terms and no diffusion terms. All these three schemes contribute to the numerical robustness, and we would not succeed in the calculation if any of these were lacked. For time advancing, the full implicit method is adopted. It requires much time to solve the band matrix equation, but numerical stability, which is quite important for nonlinear simulation, is obtained.

Several numerical results was presented to show the capability of the TASK/TX code and to confirm its validity. The benchmark test between the TASK/TX and the TASK/TR codes, the latter of which is a one-dimensional diffusive transport code, was carried out and a fairly good agreement was obtained. Several convergence studies indicated good convergence up to $\epsilon_{\rm con}=10^{-5}$. We compared the neoclassical effects, the resistivity and the bootstrap current, obtained from the steady state analysis using the neoclassical viscosity with those directly obtained from the NCLASS module and the Sauter model. It was found that our neoclassical model can describe the neoclassical effects to a reasonable extent. We also examined whether the turbulent particle diffusion model works properly through the turbulence-induced friction force and confirmed its validity. The plasma responses against the change of three parameters were studied: the turbulent particle diffusivity, the plasma current, and neutral influx. One of the important features of the TASK/TX code is to be able to describe the density profile modification dependent on the direction of the neutral beam injection, either co or counter. We examined the density and the radial electric field profiles in both co and counter cases and confirmed qualitative agreement with experimental observations on JFT-2M although turbulent transport coefficients were adjusted to reproduce the experimental values. Lastly we showed the simulation result of the radial electric field formation and the torque generation due to the ion orbit loss effect. This simulation reveals the applicability of the TASK/TX code to various problems related to radial current which cannot be treated by conventional transport codes so far.

Some subjects to be done still remain for both physical and numerical points. Physical aspects: (i) In the present formulation, we kept the lowest order term with respect to the inverse aspect ratio in surface averaging. The inhomogeneity in the toroidal magnetic field is included only in the neoclassical poloidal viscosity. For quantitative analysis, we need to keep other first order terms as well as the geometric factor due to the noncircular toroidal geometry. Further extension to the toroidal helical systems with three-dimension geometry including the toroidal viscosity is also left for future studies. (ii) We have not included the neoclassical heat flux and this neglect may be a possible cause of a discrepancy of the neoclassical effects. We have to include the equation of neoclassical heat flux in the set of transport equations. (iii) We fixed the magnitude and the profile of the particle and thermal turbulent diffusivities and viscosity. In order to carry out more comprehensive simulation, appropriate turbulent transport models should be included, such as the CDBM05 model [3] and the GLF23 model [26,41]. (iv) The transport process of neutrals should be analyzed by Monte Carlo method and multi ion species should be dealt with for an analysis of impurity transport.

Numerical aspects: The use of a cubic Hermite spline as the interpolation function of the FEM, is one of the way to increase the accuracy and the stability of the calculation further. The continuity of the derivative may enhance the robustness of the TASK/TX code required for the analyses of both edge and internal transport barriers. In order to apply the present code to a realistic tokamak plasma, we should use appropriate transport models providing turbulent transport coefficients, which depend on the density, the temperature, the safety factor and their derivatives. The CDBM05 model, which is able to reproduce the formation of ITB, is a non-stiff model and thus an analysis with the CDBM05 model will be readily achieved. The stiff transport models like the GLF23 model, however, are expected to require much smaller time step and higher accuracy; hence the TASK/TX code with cubic Hermite function is desired for the simulation with these stiff models.

Acknowledgments

The authors wish to thank Dr. T. Takizuka and Dr. N. Hayashi for the fruitful discussion on the SOL modellings and Dr. K. Shimizu for providing information on one-dimensional transport simulations including the SOL. They also wish to thank Dr. W. A. Houlberg for the use of the NCLASS module through the NTCC site. This work was supported in part by the Grant-in-Aid for scientific research, Nos. 18560790 and 19360415, from Japan Society for the Promotion of Science (JSPS) and the Grant-in-Aid for specially-promoted research, No. 16002005, from Ministry of Education, Culture, Sports, Science and Technology (MEXT).

Appendix A. Derivation of model equations

The basic equations of the TASK/TX code, Eqs. (2)–(6), are based on the set of transport equations proposed by Braginskii [8].

In the cylindrical coordinates, the continuity equation for the density $\tilde{n}_s$ is given as

$$\frac{\partial\tilde{n}_s}{\partial t}+\frac{1}{r}\frac{\partial(r\tilde{n}_s\tilde{u}_{sr})}{\partial r}+\frac{1}{r}\frac{\partial(\tilde{n}_s\tilde{u}_{s\theta})}{\partial\theta}+\frac{1}{R}\frac{\partial(\tilde{n}_s\tilde{u}_{s\phi})}{\partial\phi}=\widetilde{S}_s, \tag{A.1}$$

where the variables with tildes depend on θ and ϕ, $\widetilde{S}_s$ is the particle source term in Eqs. (22) and (23). We integrate Eq. (A.1) over θ and ϕ to obtain a flux surface-averaged equation

$$\frac{\partial n_s}{\partial t}+\frac{1}{r}\frac{\partial(rn_su_{sr})}{\partial r}=S_s, \tag{A.2}$$

where $n_s=(1/4\pi^2)\int_0^{2\pi}\mathrm{d}\theta\int_0^{2\pi}\mathrm{d}\phi\tilde{n}_s$, $n_su_{sr}=(1/4\pi^2)\int_0^{2\pi}\mathrm{d}\theta\int_0^{2\pi}\mathrm{d}\phi\tilde{n}_s\tilde{u}_{sr}$ and $S_s=(1/4\pi^2)\int_0^{2\pi}\mathrm{d}\theta\int_0^{2\pi}\mathrm{d}\phi\widetilde{S}_s$.

The equations of motion given by Braginskii were combined with the continuity equation to obtain

$$m_s\frac{\mathrm{d}}{\mathrm{d}t}\tilde{n}_s\tilde{\vec{u}}_s=-m_s\tilde{n}_s\tilde{\vec{u}}_s\nabla\cdot\tilde{\vec{u}}_s-\nabla\tilde{p}_s-\nabla\cdot\overset{\leftrightarrow}{\tilde{\pi}}_s-e_s[\tilde{n}_s\widetilde{\vec{E}}_\alpha+\tilde{n}_s\tilde{\vec{u}}_s\times\widetilde{\vec{B}}]+\widetilde{\vec{R}}_s+\widetilde{S}_sm_s\tilde{\vec{u}}_{s,\mathrm{gen}}, \tag{A.3}$$

where $\overset{\leftrightarrow}{\tilde{\pi}}_s$ is the stress tensor and $\widetilde{\vec{R}}_s$ represents the mean momentum change due to collisions with all other particles. $\tilde{\vec{u}}_{s,\mathrm{gen}}$ is not the flow velocity at a certain position but the velocity which the momentum source has when particles are generated, and the last term of the right hand side vanishes under the assumption that the mean generated velocity is zero. In the cylindrical geometry, we use the expression of the stress tensor, Eq. (15.16) in Ref. [42], and average the above equation over θ and ϕ. We assume that the variation of the physical quantities $\widetilde{X}$ on the flux surface is small, so that high order terms with respect to $\widetilde{X}-X$ may be neglected. Thus we obtain

$$m_s\left(\frac{\partial(n_su_{sr})}{\partial t}+\frac{1}{r}\frac{\partial(rn_su_{sr}^2)}{\partial r}-\frac{n_su_{s\theta}^2}{r}\right)=-\frac{\partial p_s}{\partial r}-\left(\frac{1}{r}\frac{\partial(r\pi_{srr})}{\partial r}-\frac{\pi_{s\theta\theta}}{r}\right)+e_sn_s(E_r+u_{s\theta}B_\phi-u_{s\phi}B_\theta)+R_{sr} \tag{A.4}$$

$$m_s\left(\frac{\partial(n_su_{s\theta})}{\partial t}+\frac{1}{r}\frac{\partial(rn_su_{sr}u_{s\theta})}{\partial r}+\frac{n_su_{s\theta}u_{sr}}{r}\right)=-\frac{1}{r^2}\frac{\partial(r^2\pi_{sr\theta})}{\partial r}+e_sn_s(E_\theta-u_{sr}B_\phi)+R_{s\theta}, \tag{A.5}$$

$$m_s\left(\frac{\partial(n_su_{s\phi})}{\partial t}+\frac{1}{r}\frac{\partial(rn_su_{sr}u_{s\phi})}{\partial r}\right)=-\frac{1}{r}\frac{\partial(r\pi_{sr\phi})}{\partial r}+e_sn_s(E_\phi+u_{sr}B_\theta)+R_{s\phi}. \tag{A.6}$$

In present large tokamak plasmas, a radial flow velocity is always much smaller than those in the direction of θ and ϕ: $u_{sr}\sim10^0$ m/s, $u_{s\theta}\sim10^4$ m/s and $u_{s\phi}\sim10^5$ m/s. Therefore the viscous force in Eq. (A.4) can be reasonably neglected. To obtain Eq. (3), the friction force R_{sr} is also neglected for the same reason.

As is the case with the radial equation of motion, we next consider the equation of motion in the θ-direction Eq. (A.5). The expression of the stress tensor $\pi_{sr\theta}$ is given by Eq. (15.15) in Ref. [42]. Substituting it into Eq. (A.5), we obtain

$$\frac{\partial}{\partial t}(n_su_{s\theta})+\frac{1}{r^2}\frac{\partial}{\partial r}(r^2u_{sr}n_su_{s\theta})=\frac{1}{r^2}\frac{\partial}{\partial r}\left[r^3n_s\mu_s\frac{\partial}{\partial r}\left(\frac{u_{s\theta}}{r}\right)\right]+e_sn_s(E_\theta-u_{sr}B_\phi)+R_{s\theta} \tag{A.7}$$

In addition to the momentum exchange with other particles R_θ corresponding to $F^{\mathrm{C}}_{s\theta}$ in our definition, we include the terms of the neoclassical force $F^{\mathrm{NC}}_{s\theta}$, the turbulent induced force $F^{\mathrm{W}}_{s\theta}$, the parallel loss $F^{\mathrm{L}}_{s\theta}$, the friction force $F^{\mathrm{N}}_{s\theta}$ and the charge exchange force $F^{\mathrm{CX}}_{s\theta}$ into the equation and we finally obtain Eq. (4).

We can derive the equation of motion in the ϕ-direction, Eq. (5), in the same manner of the derivation of Eq. (4) except that the neoclassical effect is not included in this equation.

The energy transport equation Eq. (6) is derived on the basis of the energy conservation law and the same as that of the conventional diffusive transport equation [43].

References

[1] R.J. Hawryluk, An empirical approach to tokamak transport, in: Course on Physics of Plasma Close to Thermonuclear Conditions, Varenna, Italy, 1979.

[2] G. Pereverzev, P.N. Yushmanov, ASTRA automated system for transport analysis, Rep. Max–Planck-IPP 5/98 (2002).

[3] M. Honda, A. Fukuyama, Comparison of turbulent transport models of L- and H-mode plasmas, Nucl. Fusion 46 (2006) 580.

[4] S.P. Hirshman, The ambipolarity paradox in toroidal diffusion, revisited, Nucl. Fusion 18 (1978) 917.

[5] T.E. Stringer, Non-ambipolar neoclassical transport, Nucl. Fusion 35 (1995) 1008.

[6] K. Itoh, S.-I. Itoh, The role of the electric field in confinement, Plasma Phys. Control. Fusion 38 (1996) 1.

[7] A.N. Brooks, T.J.R. Hughes, Streamline upwind/Petrov–Galerkin formulations for convection dominated flows with particular emphasis on the incompressible Navier–Stokes equations, Comput. Methods. Appl. Mech. Eng. 32 (1982) 199.

[8] S.I. Braginskii, Reviews of Plasma Physics, vol. 1, Consultant Bureau, New York, 1966.

[9] S.P. Hirshman, D.J. Sigmar, Neoclassical transport of impurities in tokamak plasmas, Nucl. Fusion 21 (1981) 1079.

[10] J. Wesson, Tokamaks, third ed., Clarendon Press, Oxford, 2003.

[11] A.C. Riviere, Penetration of fast hydrogen atoms into a fusion reactor plasma, Nucl. Fusion 11 (1971) 363.

[12] T.H. Stix, Heating of toroidal plasmas by neutral injection, Plasma Phys. 14, 367.

[13] R.W.P. McWhirter, Spectral intensities, in: Plasma Diagnostic Techniques, Academic Press, New York, 1965.

[14] C.S. Pitcher, P.C. Stangeby, Experimental divertor physics, Plasma Phys. Control. Fusion 39 (1997) 779.

[15] R. Hiwatari, Y. Kuzuyama, A. Hatayama, K. Okano, Y. Asaoka, S. Zhu, Y. Tomita, Simple Core-SOL-Divertor model and its application to operational space of HT-7U, J. Nucl. Mater. 337–339 (2005) 386.

[16] N. Hayashi, T. Takizuka, M. Hosokawa, Modeling of dynamic response of SOL-divertor plasmas to an ELM crash, J. Nucl. Mater. 363–365 (2007) 1044.

[17] J.M. Ogden, D.E. Post, R.V. Jensen, F.G.P. Seidl, One-dimensional transport code modelling of the limiter-divertor region in tokamaks, PPPL-1608 (1980).

[18] T. Hirayama, H. Shirai, K. Shimizu, M. Azumi, T. Takizuka, Plasma performance of limiter discharges with self-consistent plasma-wall interaction model, J. Nucl. Mater. 145–147 (1987) 854.

[19] K. Shimizu, T. Takizuka, An introduction to boundary plasma physics, J. Plasma Fusion Res. 80 (2004) 183 (in Japanese).

[20] L. Spitzer Jr., R. Härm, Transport phenomena in a completely ionized gas, Phys. Rev. 89 (1953) 977.

[21] J.D. Huba, NRL Plasma Formulary, Naval Research Laboratory, Washington, DC, 2002.

[22] L. Spitzer Jr., Physics of Fully Ionized Gases, Interscience Publisher, New York, 1962.

[23] B.A. Trubnikov, Reviews of Plasma Physics, vol. 1, Consultant Bureau, New York, 1966.

[24] S. Chandrasekhar, Principles of Stellar Dynamics, University of Chicago Press, Chicago, 1942.

[25] W.A. Houlberg, K.C. Shaing, S.P. Hirshman, M.C. Zarnstorff, Bootstrap current and neoclassical transport in tokamaks of arbitrary collisionality and aspect ratio, Phys. Plasmas 4 (1997) 3230.

[26] http://w3.pppl.gov/ntcc/.

[27] Y.B. Kim, P.H. Diamond, R.J. Groebner, Neoclassical poloidal and toroidal rotation in tokamaks, Phys. Fluids B 3 (1991) 2050.

[28] S. Inoue, T. Tange, K. Itoh, T. Tuda, Anomalous ion loss due to low-frequency instabilities, Nucl. Fusion 19 (1979) 1252.

[29] S.-I. Itoh, Anomalous viscosity due to drift wave turbulence, Phys. Fluids B 4 (1992) 796.

[30] K.C. Shaing, Neoclassical quasilinear transport theory of fluctuations in toroidal plasmas, Phys. Fluids 31 (1988) 2249.

[31] http://www.netlib.org/lapack/.

[33] W.H. Raymond, A. Garder, Selective Damping in a Galerkin Method for Solving Wave Problems with Variable Grids, Monthly Weather Rev. 104 (1976) 1583.

[34] Hayashi Nobuhiko, Isayama Akihiko, Nagasaki Kazunobu, Ozeki Takahisa, Numerical analysis of neoclassical tearing mode stabilization by electron cyclotron current drive, J. Plasma Fusion Res. 80 (2004) 605.

[35] The ITER 1D Modelling Working Group, The International Multi-Tokamak Profile Database, Nuclear Fusion 40 (2000) 1955.

[36] K. Ida, S.-I. Itoh, S. Hidekuma, Y. Miura, H. Kawashima, M. Mori, T. Matsuda, N. Suzuki, H. Tamai, T. Yamauchi, JFT-2M group, Density peaking in the JFT-2M tokamak plasma with counter neutral-beam injection, Phys. Rev. Lett. 68 (1992) 182.

[37] O. Sauter, C. Angioni, Y.R. Lin-Liu, Neoclassical conductivity and bootstrap current formulas for general axisymmetric equilibria and arbitrary collisionality regime, Phys. Plasmas 6 (1999) 2834.

[38] D.J. Ward, L–H transition theories and theory for H-mode, Plasma Phys. Control. Fusion 38 (1996) 1201.

[39] K.C. Shaing, An estimate of the ion orbit loss rate in tokamaks, Phys. Fluids B 4 (1992) 3310.

[40] K.C. Shaing, C.T. Hsu, R.D. Hazeltine, Effects of orbit squeezing on poloidal mass flow and bootstrap current in tokamak plasmas, Phys. Plasmas 1 (1994) 3365.

[41] R.E. Waltz, G.M. Staebler, W. Dorland, G.W. Hammett, M. Kotschenreuther, J.A. Konings, A gyro-Landau-fluid transport model, Phys. Plasmas 4 (1997) 2482.

[42] L.D. Landau, E.M. Lifshitz, Fluid Mechanics, Course of Theoretical Physics, vol. 6, Pergamon Press, London, 1959.

[43] F.L. Hinton, R.D. Hazeltine, Theory of plasma transport in toroidal confinement systems, Rev. Mod. Phys. 48 (1976) 239.